Water Resources Center
Annual Technical Report
FY 2007

Introduction

Research Program

Use of fluidized bed slag reactors for passive treatment of acid mine drainage

Basic Information

Title:	Use of fluidized bed slag reactors for passive treatment of acid mine drainage
Project Number:	2006OH32B
Start Date:	3/1/2006
End Date:	6/30/2007
Funding Source:	104B
Congressional District:	6th
Research Category:	Water Quality
Focus Category:	None, None, None
Descriptors:	
Principal Investigators:	Guy Riefler

Publication

USE OF FLUIDIZED BED SLAG REACTORS FOR PASSIVE TREATMENT OF ACID MINE DRAINAGE

Final Report

Guy Riefler
Department of Civil Engineering
Ohio University
Athens, Ohio 45701

Problem and Research Statement

Coal production has been a major industry in Ohio and because of increasing pressure on petroleum reserves will likely continue into the future. Mining however can have a significant negative impact on water resources, and abandoned underground mines continue to be a serious threat to water quality in southeast Ohio. Ohio coal deposits contain significant quantities of pyrite. As water and oxygen are supplied to these underground pyrite reserves by abandoned mine shafts, chemical and biological reactions oxidize the pyrite forming high concentrations of sulfuric acid and dissolved iron. The resulting low pH also dissolves other metals, typically aluminum being of greatest concern in Ohio. Water released from these mine shafts carry very high acid and metal loads that can kill aquatic life in a stream for miles downstream. For the past twenty years, southeast Ohio has devoted millions of dollars to reducing the impact of this acid mine drainage (AMD). Yet AMD remains a leading cause of surface water pollution in southeast Ohio.

One particularly difficult type of AMD source to treat occurs when a large mine complex empties near an impact point with no space for installation of a large passive treatment system. Active treatment systems are sometimes employed such as alkaline dosing, but the ongoing maintenance costs pose a problem for managing agencies. In the past five years, waste iron slag has emerged as an attractive treatment alternative. When iron ore is melted and purified, slag is the waste product that floats to the top of the melt and is discarded. It is strongly alkaline and inexpensive. When used for AMD treatment, the acidic water is directed through lined pits filled with uniformly sized pieces of slag. However, the elevated pH results in precipitation of metals, primarily iron and aluminum. The metals may clog and armor the slag which over time leads to hydraulic clogging of the slag bed and reductions in alkalinity addition. As a result, slag beds are often used only when a clean water source can be found. Thus, clean water flows through the slag bed, raising the pH to approximately 11 which is then mixed with the AMD. This is a very effective, inexpensive, and treatment option, although, it is only possible at sites with a clean water source, room for installation of the bed, and room for installation of a wetland to collect the metals precipitates before reaching the impact point.

This research tested the effectiveness of a novel treatment configuration. Fluidized bed reactors are extremely efficient, providing significant surface contact time in a very small footprint. Engineered systems like these are seldom considered for AMD treatment because of the energy requirements to fluidize the bed. However, abandoned mine flows often have sufficient pressure to provide enough head for fluidization of the bed. Further, the agitation of the slag particles will allow metal precipitates to flow out of the bed preventing clogging. It is likely that scouring of the slag particles will also prevent armoring and maintain continuous alkalinity addition, until the particles require replacement. In short, this research tests a new treatment technology that if successful will have application to some of our most troublesome AMD sources.

Methodology

The first portion of this experiment was to determine the rate at which different sieved slag fractions fluidized using a fluidized bed reactor. The reactor was composed of a large glass chromatography column 4" inner diameter and 24" length (ACE Glass Incorporated, Vineland, NJ; see Figure 1). Slag fines were supported by a plastic frit supplied with the column. Water flowed through a Materflex adjustable peristaltic pump and a flow equalizer to eliminate pulsing before entering the bottom of the column. pH into and out of the fluidized bed was measured using a WTW Multi 350i pH meter and a Denver Instrument Model 225 pH meter. Influent and effluent samples were periodically collected and analyzed for acidity and alkalinity using standard methods (Standard Methods, 20th Edition, 1998).

Slag sand was obtained from Tube City IMS (Horsham, PA), a company that specializes in slag recovery. Chemical analysis from the company indicated a pH of 12.6 and calcium carbonate equivalent of 612,000 mg/kg for the slag. Slag fines were sieved using #20, #40, and #60 sieves and the fractions were saved. These sieves have mesh sizes of 850 µm, 425 µm, and 250 µm respectively. Mine spoil or gob was collected from a local site that was known to produce significant AMD. A 20-gallon tub was filled with gob and flooded with tap water. After several days, pH and acidity in the water was 2.8 and 170 mg $CaCO_3$/L. In addition, artificial AMD was prepared to simulate measured AMD concentrations measured at a local site. Sulfuric acid was added to 50 L of tap water until pH = 5. 35.1 g of ferrous ammonium sulfate was dissolved and then more sulfuric acid added to drop the pH to 4. Target iron concentration was 100 mg/L

Four sets of tests were performed with this fluidized bed reactor. First, the three different slag sizes were tested at different flow rates to determine flow required for fluidization. Next, effluent pH with clean water running through the fluidized bed was determined. For the third test, AMD generated from the gob pile was delivered through the fluidized bed, and effluent pH and alkalinity and acidity concentrations measured. Finally, artificial AMD was treated with the slag fluidized bed. Influent and effluent concentrations were monitored with pH, alkalinity, acidity, and total dissolved iron. Fresh slag was always used for each test.

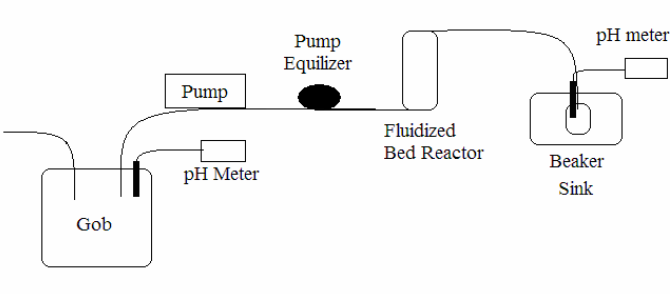

Figure 1: Fluidized Bed Reactor Setup

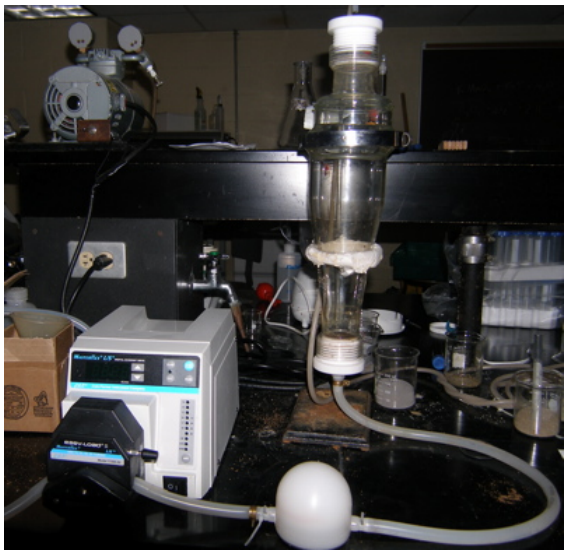

Figure 2: Peristaltic pump and fluidized bed reactor

Principal Findings

Fluidization of Slag

The first part of this project was to determine the flow rate at which different sizes of slag particles fluidize. Originally a glass frit was used, but the glass frit did not allow the fluid to flow at a sufficient rate. It was determined that the plastic frit that was provided with the original glassware produced better results. Below are the tables showing the fluidization tests with the plastic frit of slag particles from #20, #40, and #60 sieves.

Table 1: Fluidization results at different flow rates using #20 slag

Flow Rate (mL/min)	Description for 1" #20 slag layer	Flow Rate (mL/min)	Description for 1.25" #20 slag layer
100	No movement	100	No movement
200	No movement	200	No movement
300	No movement	300	There was some small shaking in a vibrating like motion.

400	No movement	400	There was some small shaking in a vibrating like motion.
500	There was some small shaking in a vibrating like motion.	500	There was some small shaking in a vibrating like motion.
600	There was little movement of small particles on top layer.	600	There was some small shaking in a vibrating like motion.
700	There was little movement of small particles on top layer.	700	There was some small shaking in a vibrating like motion.
800	There was little movement of small particles on top layer.	800	There was faster shaking in a vibrating like motion.
900	One tunnel of movement 3/4in wide.	900	There was some small movement of slag pieces in one 1in section.
1000	Single tunnel flowing faster	1000	There was faster movement of slag pieces in one 1in section.
1100	Single tunnel was about 1in wide and flowing faster. Little to no movement in other areas.	1100	Faster movement in 1.25in section. Little to no movement in other areas.
1200	Single tunnel was now about 1in wide and flowing faster. Little to no movement in other areas.	1200	Faster movement in 1.5in section. Little to no movement in other areas. Section in motion raised 1/16in.
1300	Single tunnel is now about 1in wide and flowing faster. Little to no movement in other areas.	1300	Faster movement in 1.5in section. Little to no movement in other areas. Section in motion raised 1/16in.
1400	Another section was starting to flow about 1.25in wide. Section in motion was raised 1/4in.	1400	Section in motion was raised 1/8in. 1 in of moving perimeter was fluidized.
1500	1/4 of perimeter was fluidized. Little to no movement in other areas.	1500	1.75in of perimeter was in motion. 1.25in fluidized. Little to no movement still in other areas.
1600	1/4 of perimeter was fluidized. Little to no movement in other areas. Tunnel was raised 1/4in.	1600	1.5in fluidized. Section in motion was raised 1/4in.
1700	1/4 of perimeter is fluidized. Little to no movement in other areas. Tunnel was raised a little under 1/2in.	1700	2in of perimeter was in motion. 1.5in fluidized.
1800	About 1.75in of perimeter was fluidized.	1800	1.75in fluidized. Section was in motion raised 5/16in.
1900	2in of perimeter was fluidized.	1900	Faster movement
2000	Section in motion raised 5/8in and flowed faster.	2000	Faster movement
2100	Section in motion was raised 3/4in and flowing faster.	2100	2in of perimeter was fluidized. There was little to no movement in other areas.
>2100	Fluidized section grew a little in height and the speed of flow increased with increasing flow rate. Areas not fluidized had little to no movement.	2200	Fluidized section raised 3/8in.
		2300	2.125in fluidized. Fluidized section raised just under 1/2in.

		2400	Faster motion
		2500	2.125in fluidized. Fluidized section raised just under .5in.
		2600	Fluidized section grew a little in height and the speed of flow increased with increasing flow rate. Areas not fluidized had little to no movement.

Table 1 shows that #20 slag started to have sections fluidize around 1500 mL/min. In trial 1 the maximum amount fluidized was 2 in of the perimeter, this occurred at 1900 mL/min. In trial 2 the maximum amount fluidized was 2.125 in of the perimeter and this happened at 2300 mL/min. Significant fluidization was not achieved with this size slag at any flow rate.

Table 2: Fluidization results at different flow rates using #40 slag

Flow Rate (mL/min)	Description for 1.25" #40 slag layer	Flow Rate (mL/min)	Description for 1.5" #40 slag layer
100	No movement	100	No Movement
200	One small tunnel formed with very slow movement. The slag as a whole was in a wave like vibration.	200	There was some shaking of whole mass
300	Same wavelike vibration, but faster	300	There was some shaking of whole mass
400	Original tunnel grew and was 3/4in wide. Small tunnels formed in bottom half of slag.	400	Faster shaking. There was some movement of particles in 1/4 of perimeter.
500	Original tunnels became wider. Other tunnels formed with slower flow.	500	Faster shaking. There was some movement of particles in 1/4 of perimeter.
600	1/2 of perimeter was in motion. The slag has raised 1/16in.	600	More tunnels were formed toward the top. Slag was raised 1/16in. 1/4 of perimeter had motion
700	Faster motion in perimeter. Instead of tunnels the slag was moving in sections. 2/3 of perimeter had movement	700	1/4 fluidized. There was some movement in 1/2 of perimeter.
800	1/3 of perimeter fluidized. Faster flow in other formed tunnels.	800	There was faster movement in 1/2 of perimeter. Slag has raised 1/8in
900	1/2 of perimeter was fluidized. Slag has raised 1/4in	900	1/3 of perimeter was fluidized. Faster movement in another 1/3 of perimeter. Slag had raised 3/16in.
1000	1/2 of perimeter was fluidized. Slag was raised 1/4in. There was faster movement of slag.	1000	1/3 of perimeter was fluidized. There was faster movement in another 1/3 of perimeter. Slag had raised 1/4in.

1100	2/3 of perimeter fluidized. There was faster movement of slag.	1100	1/2 of perimeter was fluidized. Slag had raised 7/8 in
1200	2/3 of perimeter was fluidized. There was faster movement of slag.	1200	2/3 of perimeter fluidized. Other areas had little to no movement.
1300	There was faster higher flow in fluidized areas.	1300	There was faster movement in fluidized areas.
1400	1/3 of slag had little to no movement. There was fast fluidization in all other areas.	>1300	Movement in fluidized areas just sped up with increasing flow rates. Areas with little to no movement remained that way.
1500	1/3 of slag had little to no movement. Fast fluidization in all other areas.		
>1500	Above 1500 flow of areas already fluidized just increases and the areas with little to no movement did not change.		

Table 2 shows that Sieve #40 started to fluidize around 800 mL/min. In both trials it shows that 2/3 of the perimeter fluidized was the maximum amount of area fluidized. This occurred around 1200 mL/min in both trials.

Table 3: Fluidization results at different flow rates using #60 slag

Flow Rate (mL/min)	Description for 1" #60 slag layer
100	Two sections showing shaking motion
200	As a whole slag raised 1/16in. 2in wide was in motion on one side. 1.5 in wide on other side. As a whole showed shaking flow.
300	1/2 of perimeter showed faster shaking motion. Slag as whole raised 1/8in. 2.25in wide tunnels raised.
400	Section in motion flowed faster. Slag as a whole raised .25in. .25in of perimeter was fluidized
500	1in of perimeter fluidized. Other areas moving faster. Other sections little to no movement.
600	About 2in of perimeter fluidized. Slag raised .5in.
700	1/2 of perimeter fluidized. Tunnels forming in sections that previously had no movement.
800	80% of perimeter is fluidized. No movement in 10% of slag.
900	85% fluidized. 10% has little to no movement.
1000	90% fluidized. 10% has little to no movement.
1100	90% fluidized. 10% has little to no movement.
>1100	There were no extreme differences in the movement of the slag after 1100 and fluidization was never reached at the speeds produced.

Table 3 shows that fluidization occurred at an even lower flow rate with the #60 slag, with the bed expanding with flow rates as low as 400 mL/min and near complete fluidization at 800 mL/min. Even at higher flow rates, however, approximately 10% of the bed never fluidized.

The previous set of experiments showed varying degrees of fluidization with different slag grain size and flow rates. Often partial fluidization would occur, that is, only a small portion of the slag layer would show significant movement, while the remainder of the layer stayed fixed.

Consequently there was not a clear demarcation for the beginning of fluidization. Further even at high flow rates, a portion of the bed always remained fixed.

These results indicate that #20 slag was too large to adequately fluidize at flow rates less than 2500 mL/min and would not be suitable for the apparatus in this experiment. We chose #40 slag at a flow rate of 800 mL/min which provided adequate movement of the particles at a flow rate that our experimental set-up could accommodate. For scaling up of the reactor to a field site, however, these results were discouraging. It required significant flow to fluidize only a 1 in thick layer of fine particle slag. The high flow rate reduces the retention time in the reactor and limits the ability of the slag to release alkalinity. Clearly a deeper layer of slag will be required; however it seems not possible to fluidize it. Also, the fine particles will likely be exhausted of alkalinity earlier than the larger slag particles.

Fluidized Bed Treatment of AMD

The first test that was conducted was running the fluidized bed reactor system with tap water and the Sieve #40 slag at a flow rate of 800 mL/min. For this test only the pH exiting the system was recorded every 20 seconds for 3000 seconds, and pH results are shown in Figure 3. Influent pH to the reactor remained near 7.2 for the duration of the experiment. Initially, pH increased over 9 but then decreased to a fairly stable value of 8.1. The initial high pH was likely due to rapidly dissolving slag fines that were quickly exhausted. The stable exit pH of 8.1 was not significantly higher than the inflow. This was likely due to the short retention time as the water flowed through the one inch layer of slag.

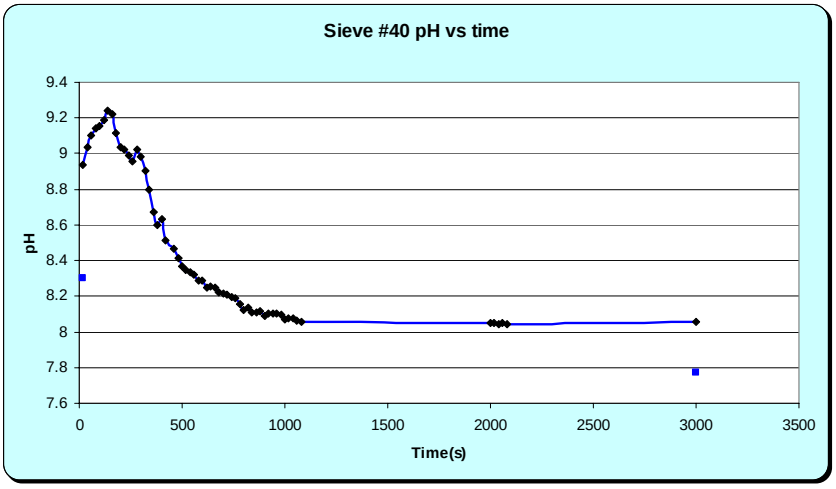

Figure 3: Effluent pH with a 1 in layer of # 40 slag, a flow rate of 800 mL/min, and tap water.

For the next test, AMD generated by the submerged gob was used as influent to the fluidized bed reactor. In order to increase retention time, a 2 in layer of #60 slag was used at a flow rate of 800 mL/min. pH measurements were taken at the entrance and exit every minute for one hour. Samples were taken at 0, 5, 10, 20 and 30 minutes and analyzed for alkalinity and acidity. pH results are shown in Figure 4, and acidity and alkalinity results are shown in Figure 5.

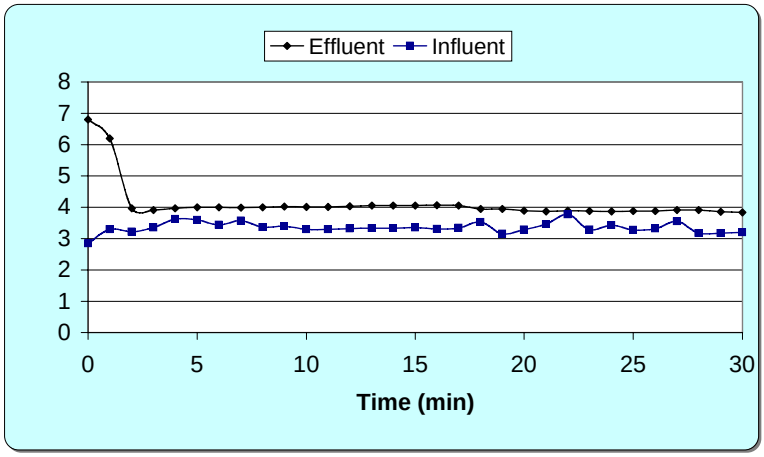

Figure 4: Influent and effluent pH with slag #60, a bed depth of 2 in, a flow rate of 800 mL/min, and acidic influent.

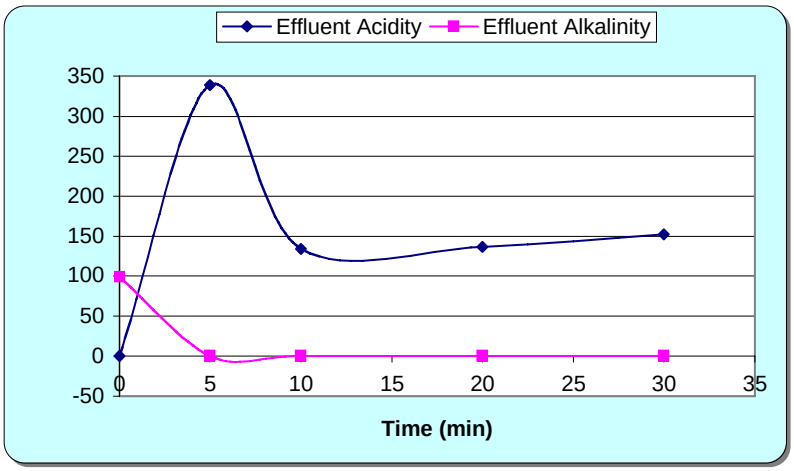

Figure 5: Effluent alkalinity and acidity plotted against the time with slag #60, a bed depth of 2 in, a flow rate of 800 mL/min, and an acidic influent.

Throughout this test the leachate from the gob averaged a pH of 3.4 and remained fairly constant while initial acidity was measured at 230 mg/L as $CaCO_3$. Surprisingly iron concentrations were very low in the leachate and orange hydrolysis precipitates were not observed in the effluent or the fluidized bed reactor. Effluent from the fluidized bed reactor showed very little pH rise, averaging 4.1 over the 30 min test (see Figure 4). Initial pH readings were above 6 but this likely represented initial mixing between clean water in the vessel and the AMD. Alkalinity and acidity results were equally discouraging (see Figure 5). Initial effluent contained 100 mg/L as $CaCO_3$ alkalinity and no acidity, but that quickly reversed with acidity as high as 346 mg/L as $CaCO_3$ being measured in the effluent. Clearly any increase in pH or alkalinity due to the slag was insignificant.

This test was repeated several days later under identical conditions, although the test was run for 60 min. pH results are shown in Figure 6, and acidity and alkalinity results are shown in Figure 7.

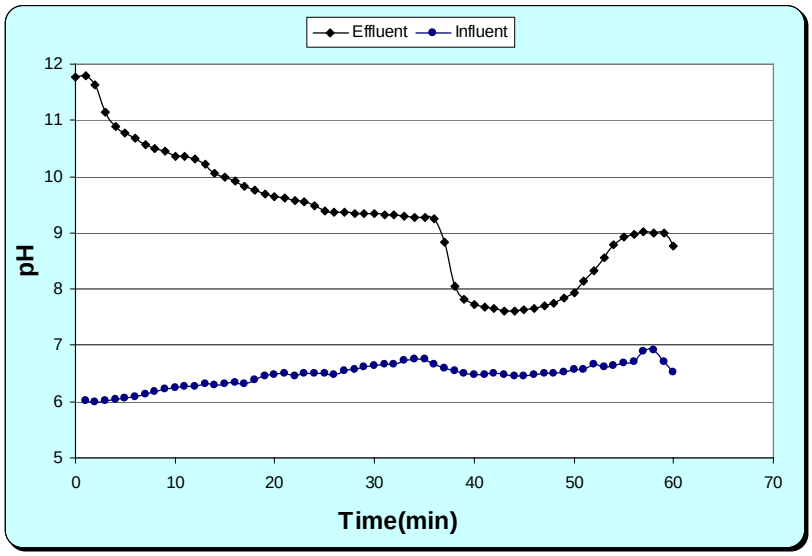

Figure 6: Influent and effluent pH with slag #60, a bed depth of 2 in, a flow rate of 800 mL/min, and acidic influent.

In this test, very high pH values were obtained in the effluent of the fluidized bed reactor, even with acidic input. Effluent pH started at near 12 but decreased gradually to a value of 7.6 after approximately 40 minutes. It did recover somewhat for unknown reasons reaching a pH of 9. The alkalinity and acidity results showed more consistent results. Initially 220 mg $CaCO_3$/L of alkalinity was generated which decreased rapidly to between 100 and 150 mg $CaCO_3$/L. Acidity was zero initially, before acidic water from the gob had reached the effluent. Acidity continually increased reaching a value of 143 mg $CaCO_3$/L by the end of the test, however it may have continued to climb beyond the test to close to the influent acidity of 170 mg $CaCO_3$/L. This residual acidity was likely in the form of hydrolysable metals that were not detected in the alkalinity test. Indeed during the hot peroxide pretreatment for the acidity test, the samples turned orange due to the oxidation and hydrolysis of ferrous iron. According to standard analytical methods the hot peroxide pretreatment step is only performed on the acidity test, not the alkalinity test, thus resulting in the seemingly contradictory result that a sample can have both positive acidity and alkalinity.

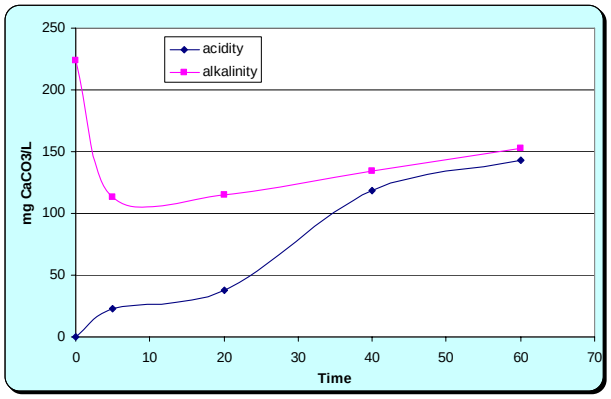

Figure 7: Effluent alkalinity and acidity plotted against the time with slag #60, a bed depth of 2 in, a flow rate of 800 mL/min, and an acidic influent.

Comparing the two tests with gob leachate, the leachate for the second test was much less severe than the first test. pH raised from 3.4 to 6.6 and acidity dropped from 230 mg/L as $CaCO_3$ to 170 mg/L as $CaCO_3$. Further tests confirmed that the gob was no longer producing sufficient acid particularly at a flow rate of 800 mL/min. In addition, the gob leachate never had sufficient iron concentrations to properly simulate AMD. As a result, artificial AMD was prepared for the remaining tests.

For the following test an acidic solution was created using tap water, dissolved ferrous iron, and sulfuric acid as the influent to the fluidized bed reactor. A 1.5 in layer of #40 slag was used at a flow rate of 800 mL/min. pH measurements were taken at the entrance and exit every minute for one hour. Samples were taken at 0, 5, 20, 40 and 60 minutes and analyzed for alkalinity and acidity. pH results are shown in Figure 8, acidity and alkalinity results are shown in Figure 9, and iron results are shown in Figure 10.

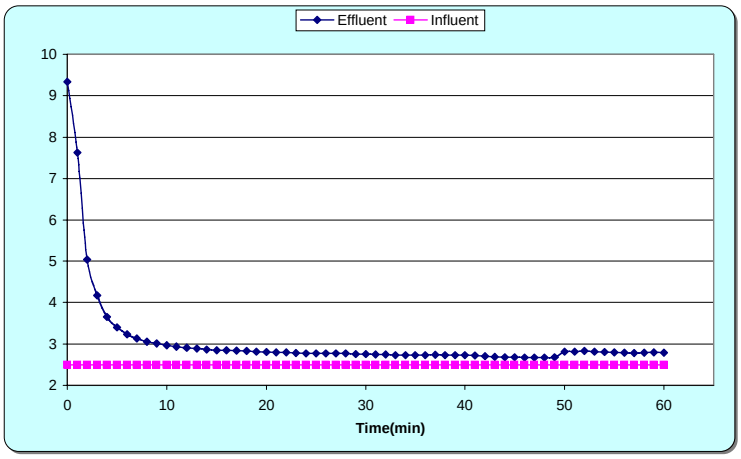

Figure 8: Influent and effluent pH with slag #40, a bed depth of 1.5 in, a flow rate of 800 mL/min, and artificial AMD influent.

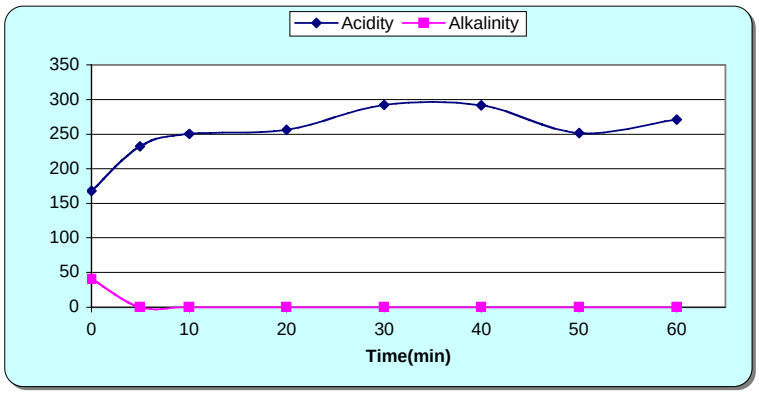

Figure 9: Effluent alkalinity and acidity plotted against the time with slag #40, a bed depth of 1.5 in, a flow rate of 800 mL/min, and artificial AMD influent

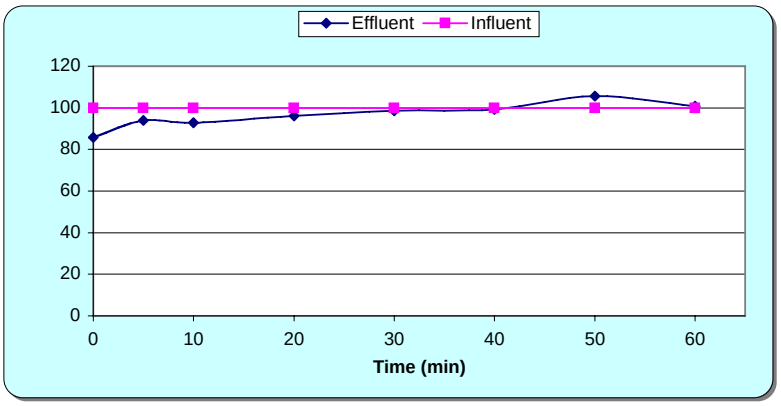

Figure 10: Effluent and influent dissolved iron plotted against the time with slag #40, a bed depth of 1.5 in, a flow rate of 800 mL/min, and artificial AMD influent

Results with the artificial AMD were similar to previous results with gob generated AMD. Influent to the fluidized bed reactor was more typical of AMD with pH of 2.5, acidity of 260 mg/L as $CaCO_3$, and ferrous iron of 100 mg/L. As before, after approximately 10 min, effluent concentrations mirrored influent concentrations for pH, acidity, and iron. Initially, some of the AMD appeared to have been neutralized by the slag, however this may have simply been mixing of the AMD with initially clean water in setting up the fluidized bed reactor.

The same test was repeated under identical conditions with the artificial AMD and results for pH, alkalinity, acidity, and iron are shown in Figures 11, 12, and 13.

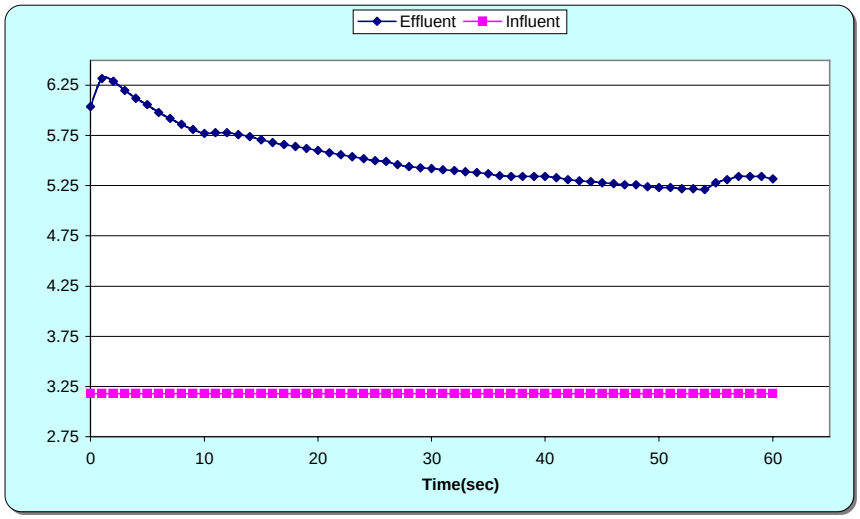

Figure 11: Influent and effluent pH with slag #40, a bed depth of 1.5 in, a flow rate of 800 mL/min, and artificial AMD influent.

In this test, the slag significantly elevated pH values obtained in the effluent of the fluidized bed reactor (see Figure 11). Influent pH averaged 3.1, while effluent pH averaged 5.4. The effluent pH started around 6, but gradually decreased to a value a little less than 5.25 around 55 minutes. It was not clear why this test of the slag with artificial AMD performed significantly better than the previous test. It could be speculated that channeling in the slag impaired results in the first test, though there was no visual evidence for this.

The alkalinity and acidity results shown in Figure 12 were far less encouraging. Initially alkalinity was generated at 132 mg $CaCO_3$/L. This value rapidly decreased to 5.6 and fluctuated slightly reaching a high value of 25 mg $CaCO_3$/L at 30 minutes before arriving at 0 mg $CaCO_3$/L for the remainder of the test. Acidity started out close to zero, but gradually rose to a high value of 176 mg $CaCO_3$/L at 40 minutes where it remained fairly steady. Again, results from this test were superior to the previous test, showing some signs of acidity neutralization and alkalinity generation. However, after the initial 40 min, slag no longer had a significant impact on effluent acidity.

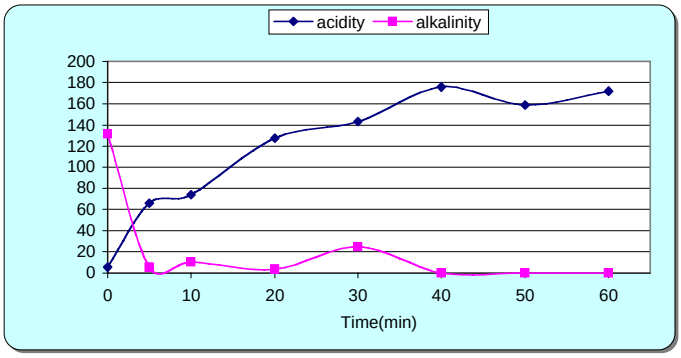

Figure 12: Effluent alkalinity and acidity plotted against the time with slag #40, a bed depth of 1.5 in, a flow rate of 800 mL/min, and artificial AMD influent

Finally, iron concentrations behaved like the acidity, with initial removal of iron but with effluent concentrations approaching influent concentrations by the end of the experiment. Iron was not directly removed by the slag, but ferrous iron oxidation was dependent on pH. As pH increases so does iron oxidation rates. At these pHs ferric iron was relatively insoluble so once oxidized, the resulting ferric iron would rapidly precipitate. In fact, after the 60 min test with artificial AMD the slag was noticeably orange in color from the iron (see Figures 14 and 15). In comparison, no iron floc was observed in the effluent from the reactor. This provided discouraging evidence for a hypothesis of this work. It was expected that fluidized beds would be able to resist clogging because the motion of the slag would release light floc from the bed and grinding of the particles would keep the slag clean and free of armoring. It appeared from this 60 min test that the iron precipitated directly on the surface of the slag rather than forming flocs, and the slag was clearly not protected from this surface precipitation. Most likely after surface precipitation sites were used independent iron floc would form, though this test was to short to confirm. It is still possible that the bed would remain mobile and release the floc, though there was no evidence of that from these experiments. Further it does appear that armoring would be a problem limiting alkalinity generation from the slag, even if the slag remained mobile.

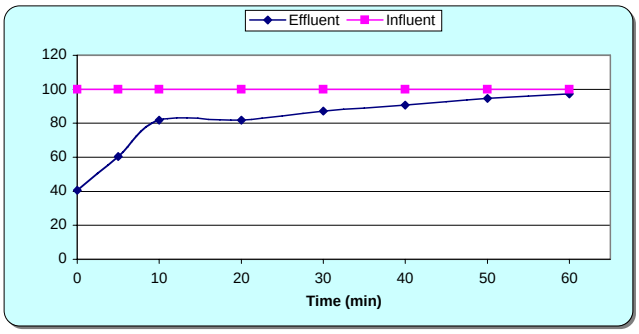

Figure 13: Effluent and influent dissolved iron plotted against the time with slag #40, a bed depth of 1.5 in, a flow rate of 800 mL/min, and artificial AMD influent

Figure 14: Wet #40 slag from the fludized bed reactor after 60 min of 800 mL/min flow with artifical AMD on left compared with fresh #40 slag on the right.

Figure 15: Dry #40 slag from the fludized bed reactor after 60 min of 800 mL/min flow with artifical AMD (left), dry #40 slag from the fludized bed reactor after 60 min of 800 mL/min flow with gob leachate (middle), and fresh #40 slag (right).

Significance

These results indicate that this treatment approach has significant limitations both with regard to hydraulics and chemical transport. First, the slag particles proved difficult to fluidize requiring the use of very small grain size. #20 slag was too large to adequately fluidize, although #40 slag and #60 slag could be adequately fluidized with bed depths of 1-2 inches. For scaling up of the reactor to a field site, these results were discouraging. These particles are extremely fine and would likely increase costs significantly to crush and sieve the slag material to this size window for full-scale implementation. Further, it required significant flow to fluidize only a 1 in thick layer of fine particle slag. The high flow rate reduces the retention time in the reactor and limits the ability of the slag to release alkalinity. Clearly a deeper layer of slag will be required; however it seems not possible to fluidize it. Also, the fine particles will likely be exhausted of alkalinity earlier than the larger slag particles.

The water chemistry results were equally discouraging. With a 1 inch layer of #40 slag, pH of tap water was increased only to around 8.1 from 7.2, not a very significant improvement. Further experiments were conducted with 2 inch layers of #60 slag. When treating AMD generated from gob leachate, pH and acidity was not neutralized except for in the initial few minutes of the test. In a second test better results were achieved, however it was determined that the gob leachate had decreased in severity. Additional experiments with artificial AMD produced similar results, with virtually no change in pH, acidity or iron concentrations after 40 min. Some initial acid neutralization and iron removal was observed initially, but again not to a significant degree. Finally, slag from the fluidized bed reactor treating artificial AMD was coated with ferricoxyhydroxide precipitates which might indicate armoring over the long term. Iron floc was not observed over the 60 min experiment.

From these experiments, it appears that a slag layer small enough to achieve reasonable fluidization was not able to treat AMD significantly, and deeper slag layers face hydraulic limitations preventing fluidization.

The Scour and Deposition River and Estuarine Bridges

Basic Information

Title:	The Scour and Deposition River and Estuarine Bridges
Project Number:	2006OH39B
Start Date:	3/1/2006
End Date:	2/28/2008
Funding Source:	104B
Congressional District:	15th
Research Category:	Engineering
Focus Category:	Geomorphological Processes, Sediments, None
Descriptors:	
Principal Investigators:	Diane L Foster, Thomas C Lippmann

Publication

1. Hatton, K. A. and Foster, D. L., 2006, Vertical Pile Scour Induced by Random Free Surface Gravtiy Waves, in 30th Int. Conf. Coastal Engin. ASCE.
2. Hatton, K. A. and Foster, D. L., 2007, Scour and Ripple Migration Offshore of a Vertically Mounted Pile Subjected to Irregular Waves, Journal of Hydraulic Engineering, ASCE, in review.
3. Hatton, K. A. 2006, Vertically Mounted Pile Scour Subjected to Irregular Waves, M.S. Thesis, The Ohio State University. Dept. of Civil and Environmental Engineering and Geodetic Science, The Ohio State University. Columbus, OH.
4. Hatton, K.A., D. L. Foster, P. A. Traykovski, P.A., and H. D. Smith, 2008, Scour and Burial of Submerged Mines in Wave Conditions, IEEE-Journal of Ocean Engineering, in press.
5. Smith, H. D., and D. L. Foster, D.L., 2005, Modeling the Flow around a Cylinder above Scoured Bed, ASCE Journal of Waterway, Port, Coastal and Ocean Engineering, 131(1), 14-24.
6. Hatton, K. A., and D. L. Foster, 2004, Scour and Burial of Submerged Mines in Wave Conditions, Eos Trans. AGU, 85(47), Ocean Sci. Meet. Suppl., Abstract OS21B-1222.
7. Foster, D. L., H. D. Smith, and K. H. Hatton, 2004, Modeling the 3-D Flow around a cylinder, Mine Burial Workshop, Woods Hole Oceanographic Institution, MA.

The Scour and Deposition around River and Estuarine Bridges
Final Report

Principal Investigators:
T. C Lippmann and D. L. Foster
The Ohio State University

Abstract

This report gives the results of a three-year effort directed at increasing our understanding of sediment scour and deposition surrounding bridge piers exposed to wave and mean flows. A combined numerical and observation effort resulted in new techniques for more accurately resolving the flow and bed evolution surrounding submerged objects. Results from this study may be used to select locations for future sampling sites, and to identify those sites where scour is expected to be problematic for future structural integrity. Our field and modeling methods represent new ways to monitor and evaluate bridge scour, and together these model-data results will highlight potential areas of concern.

Introduction

This investigation was motivated by the amount of river, estuarine, and coastal infrastructure that is susceptible to extreme wave and flooding events. The high velocities and resulting shear stresses associated with high flow velocities are capable of scouring or depositing large quantities of sediment around hydraulic structures. Preventing the failure of these structures and sedimentation in inlets alone costs federal and state agencies billions of dollars annually. In addition to being costly, the manual monitoring of bridge scour - as mandated by the Federal Highway Administration - can be inefficient in states such as Ohio where the flood events that initiate the scour process occur sporadically. According to the National Scour Evaluation Database, there are 23,326 bridges over waterways in the state of Ohio, of which 5,273 are considered “scour susceptible” and 191 are considered “scour critical”.

Related to problems generated by sediment scour are issues of sediment deposition in navigational channels. On the Maumee River, OH, alone, the Army Corp of Engineers spends millions of dollars annually to dredge an average of 850,000 cubic yards of sediment. With the elimination of open lake disposal of dredged sediments, an inter-agency collaboration of government and private citizens has been formed to identify possible methods for reducing the amount of deposition by reducing the soil erosion along river banks. Clearly, an increase in our understanding of how sediment is scoured or deposited around structures will improve our ability to utilize available resources in the most efficient manner.

Previous methods for identifying bridge scour have relied on the manual (diver-based) sampling of local water depths that are generally limited to periods of low water flow. As the dynamic scour and deposition of sediments around structures is highest during periods of high flow, traditional sampling methods have limited our ability to predict quantitatively

scour or deposition levels and to evaluate sediment transport models.

The objectives of this research were to increase our ability to predict how variations in flow conditions affect the scour and/or deposition of sediment around bridge piers. We have approached this objective through a combination of pilot field observations, detailed laboratory observations, and three-dimensional numerical simulations. This synergistic effort will ultimately allow results derived from small-scale numerical model and laboratory studies to field applications.

Methodology

Model

In this work, we simulate the flow and sediment transport field surrounding submerged objects in both wave and current dominated flows with FLOW-3D (Flow Science, Inc., Santa Fe, NM), a robust three-dimensional, non-hydrostatic computational fluid dynamics (CFD) numerical model that solves the nonlinear Navier Stokes equations (*e.g.*, Chopakatla, *et al.*, 2008). FLOW-3D incorporates one of several closure schemes, including large eddy simulations (LES) and *k-e* models, to resolve fine scale turbulence and dissipation throughout the domain. FLOW-3D uses a fixed rectangular grid (Eulerian approach), and overcomes the problem of incorporating geometry in a structured gird by using the trademark Fractional Are Volume Obstacle Representation method (FAVOR; FLOW-3D manual, 2002). The primary strength of FLOW-3D is its ability to accurately resolve three-dimensional flows in great detail, while tracking complex fluid behavior at flow-structure and flow-sediment interfaces, allowing coupled fluid-sediment equations to be incorporated. The sediment transport module of FLOW-3D is based on the bulk conservation of mass with an advection/diffusion scheme coupled with the interface tracking capabilities of the Volume-of-Fluid (VOF; Hirt and Nichols, 1981) scheme for bed level tracking. This method differs significantly from traditional sediment transport models as the grid is not fitted or regenerated to match morphology changes.

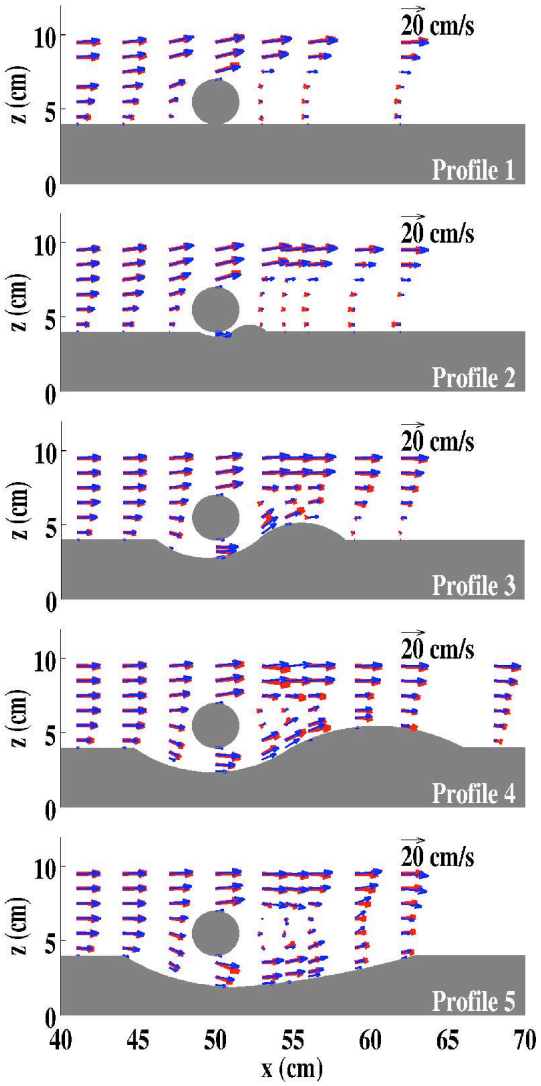

Figure 1. Observed (blue) and simulated (red) velocity profiles around a two-dimensional pipeline over 5 bed static-bed profiles. The model resolves the recirculating region present on planar and near-planar beds (profiles 1 and 2) and vortex shedding present on present on scoured beds (profiles 4 and 5).

Laboratory

Laboratory observations of the wave-induced flow field, suspended sediment, and morphologic response surrounding a vertical pile were obtained at the collaborative 2005 CROSSTEX prototype laboratory experiment held at the O. H. Hinsdale Research Lab in Corvallis, OR. The laboratory facility is 104 *m* long, 3.7 *m* wide, and 5 *m* deep, and capable of generating prototype scale random wave fields with greater than 1 *m* wave heights impinging on a sloping beach with a single, subtle sand bar approximately 40 *m* from the shoreline. In our experiments, the evolution of the flow field and seabed offshore of a vertical pile was observed under both random and monochromatic waves in the shoaling region (seaward of the breakpoint) in approximately 1.5 *m* water depth. A 6 *cm* diameter pile was hydraulically jetted vertically into the bed composed of a mixture of quartz sand with median grain size diameter of 0.19 *mm*. An underwater Particle Image Velocimetry (PIV) system consisting of a 1 mega-pixel digital camera focused on a two-dimensional laser sheet oriented along the tank in the direction of the shoreward propagating wave field was used to observe the two-dimensional (*x*-*z*) time dependent flow fields at 3 *Hz*. A two-axis variable-frequency acoustic backscatter sensor observed the sediment suspension at 1 *cm* range bins over the *x*-*z* plane, as well as the bed geometry over a 1 *m* range in the *x*-*y* plane. Figure 2 shows a sketch of the instrument deployment. Scour simulations were performed for offshore wave heights ranging from 20 to 40 *cm* with wave periods ranging from 4 to 6 *sec* for both regular and irregular waves.

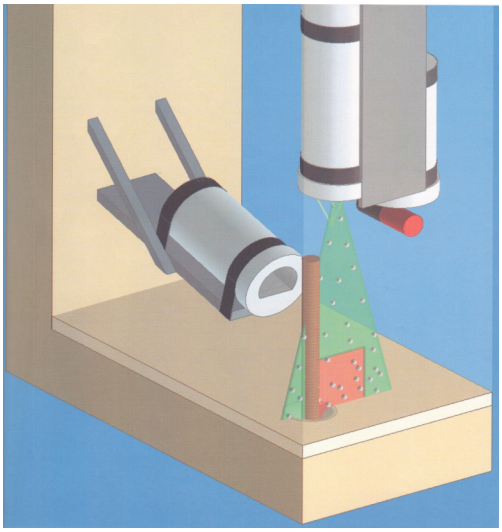

Figure 2. A sketch of the CROSSTEX laboratory deployment. The red highlight box shows the location of PIV observations of velocity and scour. The location of the two-axis sonar is identified with the red and black cylinder in the mid-water column.

Field

The riverbed topography upstream, downstream, and right at one of the support piers of a bridge located on the Great Miami River (ODOT ID-BUT-128-0855) in Hamilton, OH, was observed under high flow using state-of-the-art acoustic survey instrumentation. The river bottom topography was measured with a bathymetric survey system consisting of a Yamaha GP1200 waverunner equipped with differential GPS receiver, dual-transducer sonic altimeter, and custom navigation

Figure 3. The waverunner survey system is capable of measuring water depths from approximately 0.4 m to 15 m.

software (Figure 3). As part of previous research efforts, the system has been utilized extensively in coastal marine and fresh water environments where waves and currents are present (and sometimes energetic). The system has accuracies of about +/- 5-7 *cm* in both the horizontal and vertical coordinates of the measured bathymetry.

The local deposition upstream of one of four bridge piers was measured with a rotating two-axis IMAGENEX profiling sonar attached to the upstream side of a bridge pier. The sonar resolved the two-dimensional centimeter-scale bathymetric variations over a 5-20 *m* radius. Figure 4 shows the IMAGENEX sonar system attached to the upstream side of the ellipsoidal pier for deployment on 30 November 2005.

Figure 4. Snapshot of an IMAGENEX deployment at the proposed Hamilton site (ODOT ID-BUT-128-0855). Figure courtesy of Dave Straub (USGS).

Results

Model

The CFD model (FLOW-3D) was evaluated for two-geometries, (1) a short, horizontally oriented cylinder placed on and near the bed and exposed to both steady and oscillatory flow similar to environments with both surface waves and mean flows, and (2) a vertical pile embedded into the bottom and exposed to steady flow similar to that found in unidirectional river flow.

In the first numerical study, the short-cylinder simulations were run in a small domain approximately 1 *m* horizontally and 15 *cm* vertically with dense, O(*cm*), grid cells. The simulations were repeated over differing seabed geometries that were fixed in time and space and thus not allowed to evolve (*i.e.*, no sediment transport was allowed). The mean flows averaged over about 1 *min* time period are compared with laboratory observations obtained by Testik, *et al.* (2005) over similarly sized cylinders and bed topographies that approximately matched the idealized geometries used in the simulations. Results show for the first time that the LES model is able to accurately reproduce the vortex shedding surrounding near bed structures (Smith and Foster, 2006). Results from this work were used in a recent follow-up study, in which the model was evaluated with field observations of submarine scour around a horizontally oriented cylinder placed in 15 *m* water depth on the continental shelf offshore of Martha's Vineyard in 2005. Results (non shown) indicate that FLOW-3D accurately predicts the scour and depositional regimes from an undisturbed flat bed (Hatton, *et al.*, 2006).

In the second numerical study, steady unidirectional flow surrounding a vertical pile of 56.3 *cm* diameter was simulated and compared qualitatively to laboratory observations. In this work, the three-dimensional flow field was computed over a domain with 11.5 *m* length (downstream direction), 5.9 *m* width (cross-stream direction), and 1.7 *m* height. The grid

dimensions varied with coarser cell volumes (cubes with 9.0 *cm* sides) at the edges (far field relative to the pile) and finer cell volumes (cubes with 1.8 *cm* sides) near the pile to better resolve the flow near the pile while speeding up the simulation run time without loss in resolution of flow structure. The flow was initiated at the upstream (inflow) boundary with steady mean currents of 32.6 *cm*/*s*. A continuous outflow boundary condition at the downstream end of the domain was specified that minimized wave reflections. The bottom boundary condition allows no flow through the bottom, and contains small roughness elements needed for numerical stability. The surface boundary condition was specified as rigid lid (no temporal variations in the sea surface elevation). Figure 5 shows both downward and sideward looking predictions of the velocity field. In this case, the water depth was twice that of the pile diameter. Upstream of the pile, the simulations show a region of high stress induced by the presence of a horseshoe vortex, visual in the figure by the velocity magnitudes larger than the undisturbed flow. The presence of the horseshoe vortex suggests a region where sediment will be removed and the potential for a scour hole to develop on the upstream side of the pile. On the other hand, downstream of the pile the mean flow field shows lower velocities than the undisturbed flow suggesting a region where sediment would be deposited. Interestingly, the simulations predict the presence of vortex shedding downstream of the pile, which should decrease the depositional regimes.

Laboratory

The nature of the complex flow field modeled with FLOW-3D, characterized by an erosional regime on the upstream side of the pile and with potentially competing accretional and depositional regimes downstream of the pile, is qualitatively evaluated with laboratory observations obtained as part of the CROSSTEX experiment. The fluid forcing for the model was determined by the observed free stream flow during CROSSTEX, and thus shows the predicted bed changes that would arise from flow patterns initially over a featureless, flat bed with no scour hole or depositional wedge by the pile. Figure 6 shows two snapshots of the velocity field in the *x*-*z* plane over a 22 *cm* x 22 *cm* region just offshore (upstream) of the pile. The snapshots occur at the start and end of the 20 *min* experiment. At the beginning of the run, a stagnation point eddy was qualitatively observed at the sediment-pile interface (not shown in the figure). At the equilibrium bed state (which occurred at 26 *min* into the run), the bed has developed ripples and a 3 *cm* scour hole has developed around the upstream side of the pile. This bed change is qualitatively consistent with the predicted bed changes from the model simulations.

The modeled flow field will be quantitatively evaluated with the CROSSTEX observations in a similar manner as with the horizontal cylindrical experiments (Smith and Foster, 2005). Preliminary results (Figure 7) show that the scour depth, *S*, relative to the vertical pile diameter, *D*, is increases for increasing wave period (T) but is relatively insensitive to wave period or the narrowbandedness of the wave spectrum. This investigation yielded two new findings. First, the presence of bedforms had a significant impact on the scour development. As bedforms migrated towards the evolving scour hole, both scour evolution and bedform migration would temporarily cease when the bedform crest was within one-half a wavelength of the edge of the scour pit. Figure 8 shows a time stack of bedform migration towards an evolving scour hole. The Figure shows a stall of scour evolution and bedform migration as the bedform crest approaches the pile. This suggests

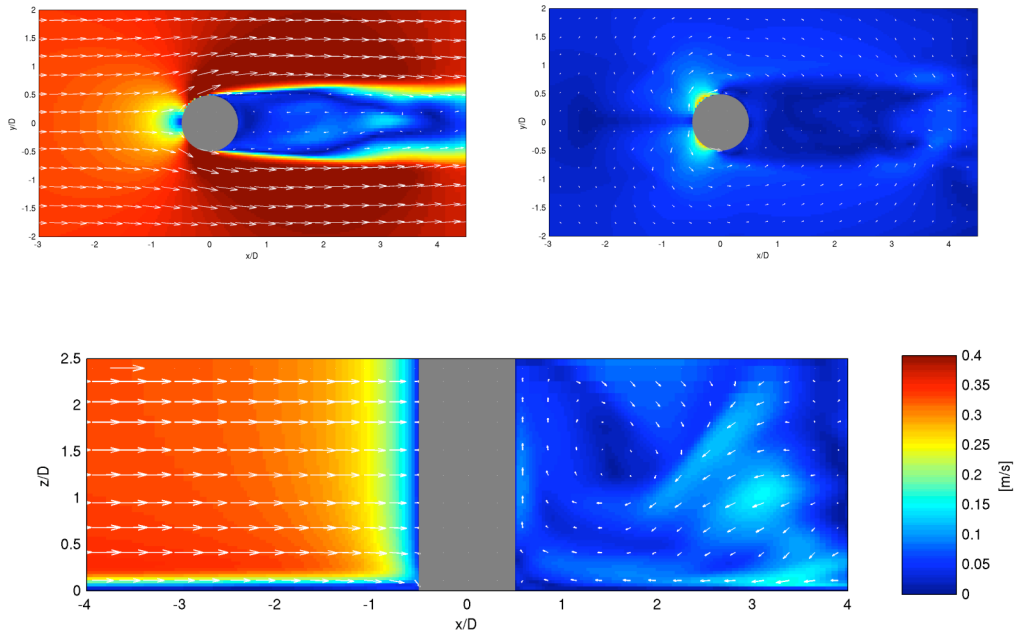

Figure 5. (top panels) Mean of the modeled flow around a vertical pile, viewed from above, and taken at a depth of (right panel) one pile diameter and (left panel) at the bed. (bottom panel) Mean of the modeled flow around a vertical cylinder, viewed from the side at the centerline of the pile. The pile diameter, *D*, is 53.6 *cm*. The along-tank (horizontal axis) and cross-tank (vertical axis) dimensions are scaled by the pipe diameter, D. Flow is traveling from left to right in the figure, with a mean velocity of 32.6 *cm*/*s*. The gray shaded area represents the pile, while the color map indicates the velocity magnitude (*cm*/s). Vectors indicate velocity and are scaled by the single vector appearing in the upper left-hand corner of the image representing a 40 *cm*/*s* velocity.

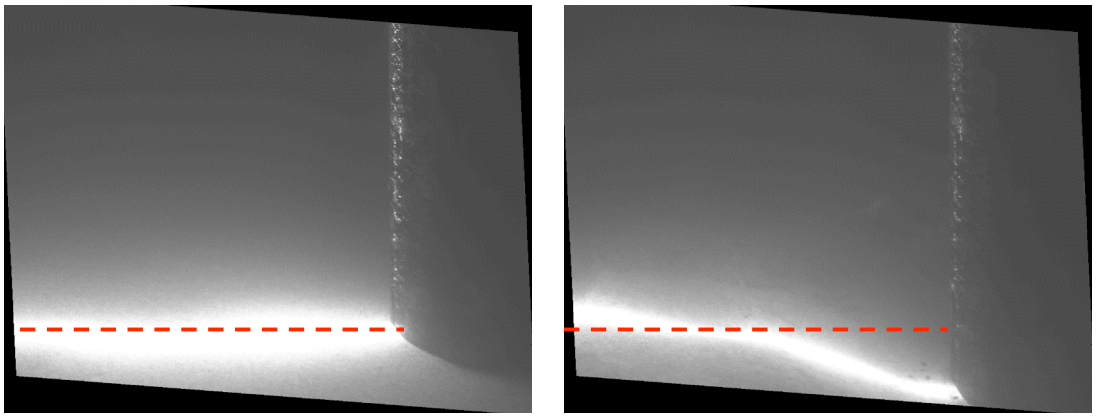

Figure 6. The (right panel) initial and (left panel) final bed profile offshore of a vertical pile measured with the PIV system during the CROSSTEX experiment. The bed elevation indicated with the bright light reflected from the bed. The pile is indicated as the dark gray ar on the right of each image. The red dashed line indicates the position of the initial bed elevation.

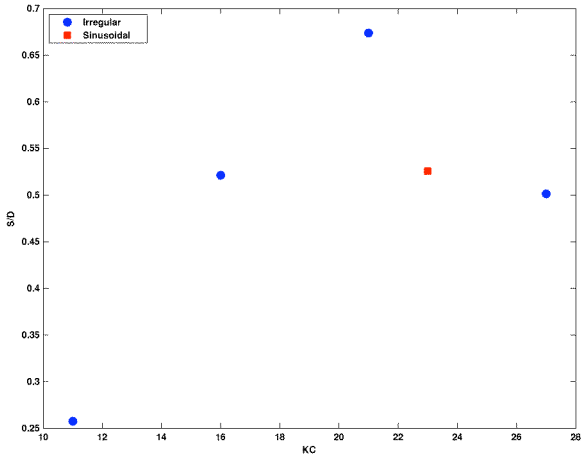

Figure 7. The final scour depth (non dimensionalized by the pile diameter) versus th Keulagan-Carpenter number, where KC=UT/D.

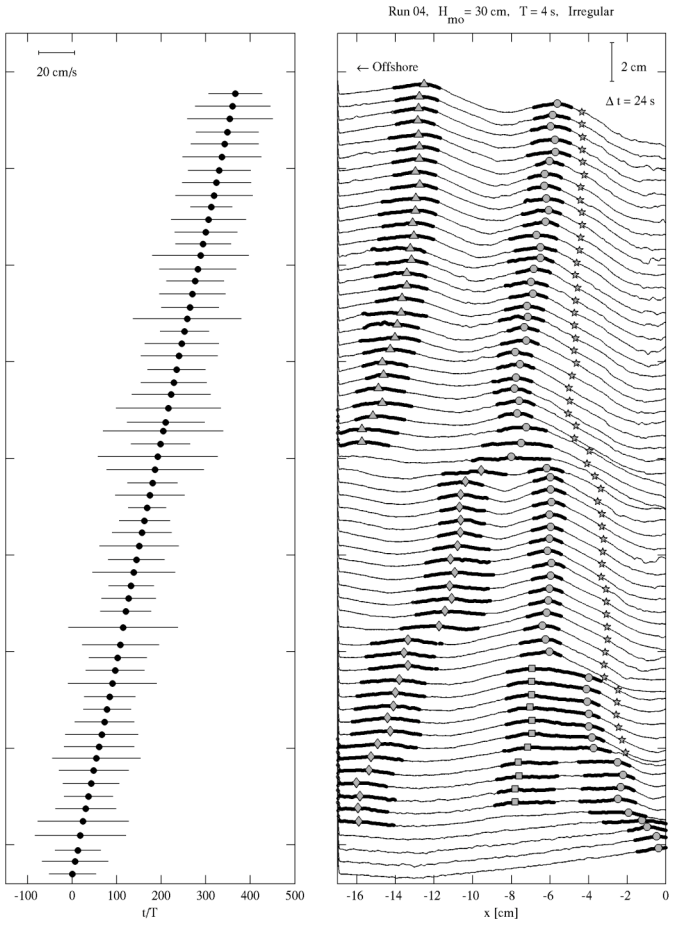

Figure 8. Bed profiles and forcing for a 30cm significant wave height and 4 sec. irregular wave peak period (T). (a) The non-dimensional time (t/T) of each of the bed profiles in (b). The horizontal lines represent the standard deviation of the near-bed horizontal velocity during each averaging window. (b) Bed profile time stacks. Local maxima are represented with open symbols. The outer edge of the developing scour hole is represented with the circular symbol.

temporary cessation of sediment transport in response to the turbulent structure interactions between the pile and boundary layer. Second, observations of scour development and bedform migration for regular waves evolved significantly differently than observations under irregular waves. Under regular waves, the bed forms migrated 5 times faster than under comparable energy irregular waves. This suggests significant difficulties in translating regular wave laboratory studies to natural environments.

Field

Figure 9 shows images of our waverunner survey of the Great Miami River at Hamilton obtained on 30 November 2005. Both figures show color contours of the bathymetry, with the left panel showing the survey tracks from the waverunner as well as a walking GPS survey of the river banks. The right figure shows the location of the pier piling edges (as circles) and the locations of cross-river transects where comparisons to a USGS 1999 survey can be done. The elevations of the river banks in the plots are omitted because the high elevation of the banks obscures the details of the subsurface river topography.

The horizontal (x, y) coordinates are in meters relative to our established GPS base position. North is toward the top of each figure. The vertical elevations (given by the color contours defined by the scale on the right-hand-side of the figures) is also in meters relative to the mean waterline elevation observed by the waverunner averaged over the whole survey length. The elevations were transformed in this manner so that the approximate water depths are given. The actual coordinates before transformation are in the ITRF00 reference frame. Note that the cross-river and along-river scales are not the same, with the cross-river scales exaggerated by a factor of 2 for visual clarity.

The survey spans about 1.2 *km* along the river, and was done over 2.5 *hrs* with about 60 cross-river transects spaced every 20 *m*. We were also able to get close to the river's edge owing to the relatively steep banks. The bridge where the Imagenex sonar was deployed (see Figure 4) is located about $y = 200$ *m* in the plot. There is a gap in the tracks where the bridge is located as we were only able to get within about 10 *m* or so of the bridge before the GPS satellites were blocked. The raw survey data were smoothed onto an evenly spaced grid and interpolated beneath the bridge; however, the accuracy of the water depths under the bridge is not known owing to potential largish changes right by the bridge pilings. Techniques are presently being developed that will allow for accurate surveys everywhere beneath the bridges (based on dead-reckoning navigation of along-river waverunner transects).

The river bed topography shows significant variability. For example, about 200 *m* downstream (south) of the bridge there are deep holes (up to 4.5 *m* depths) on the west side of the river, whereas on the east side there is a shallow bar that extends toward the middle as you move downstream. The cross-river gradient is about 1:20 at about $y = 0$ *m*. There also appears to be a shallow bar on the western bank toward the northern end of the survey (about 400 *m* upstream of the bridge) and a general deepening of the river toward the south (about 600 *m* downstream of the bridge).

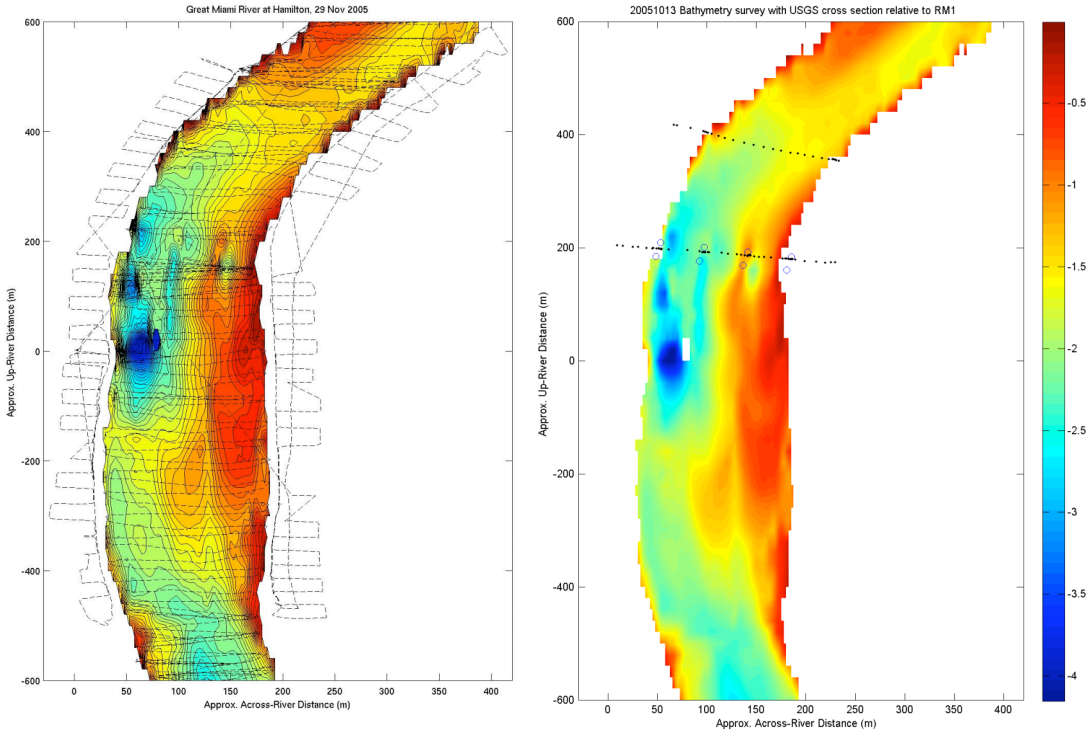

Figure 9. Bathymetric survey of the Great Miami River in Hamilton, OH, conducted on 29 Nov 2005. The depths are shown in meters as color contours relative to the approximate mean water level at the bridge (located at about *y* = 200 *m* in the figure). The horizontal coordinates are in meters relative to our GPS base position. The bridge pilings are shown as circles in the right-hand panel located an across-river distance of approximately *x* = 130 *m*. The survey tracks are shown as dashed black lines in the left panel. The riverbanks exceeding 6-8 meters above water level were surveyed with differential GPS manually (*e.g.*, walking) but are omitted from the plot so that the river topography can be seen more clearly. The location of cross-river transects compared with USGS surveys (Figure 9) is shown in the right-hand panel.

It would be expected that highly variable flow over the inhomogeneous river topography would result in significant changes in the river morphology over time, with inter annual variability approaching meter scale in some instances. Limited survey data exists to compare with our surveys, particularly of the dense grid scales obtained with our state-of-the-art survey system. Still, in 1999, two cross-river transects were conducted by the USGS. A comparison between these data and our 2005 survey is shown in Figure 10. Owing to uncertainties in the USGS vertical origin, the USGS data is offset 14 *m* vertically in the figures. Although there is some cross-river depth variation observed between 1999 and 2005, the general characteristics of the profile are retained. The general agreement in location of the river bank at the edge of each survey indicates that the vertical offset applied to the USGS data is reasonable, and that changes to the river bed topography have not been substantial. As no surveys were done downstream of the bridge, no comparison to the downstream profiles can be made with the 2005 survey. Plans to resurvey this section of river periodically are under way and a part of ongoing research efforts.

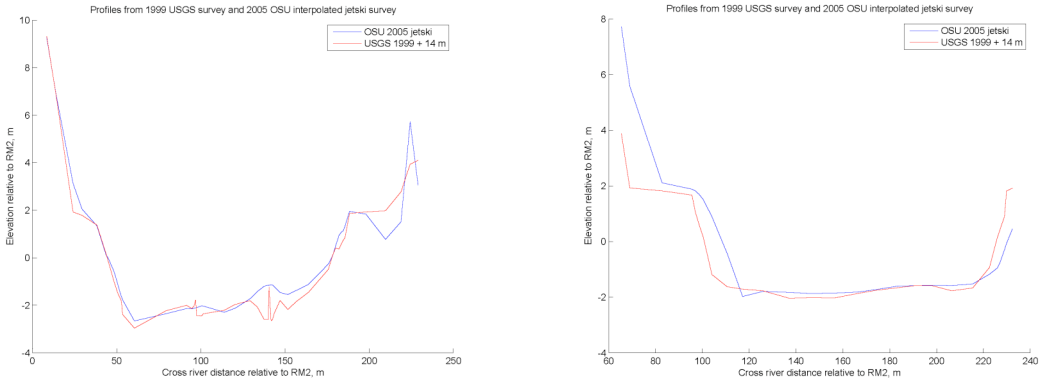

Figure 10. Comparison of 2005 across-river topography obtained by our GPS-based waverunner survey system with a 1999 survey conducted by the USGS. The locations of the transects are shown in Figure 7. Owing to uncertainties in the origin of the USGS survey, the coordinates for the USGS surveys were offset vertically 14 *m* to approximately match that of the waverunner surveys. After adjustment, little change in the river topography upstream of the bridge was observed in the 6 years between surveys. Note that no USGS surveys were done downstream of the bridge so no comparisons with our 2005 survey could be done.

The river bed geometry just upstream of one of the pier pilings was observed with the Imagenex sonar system for about a 2 *hr* period on 30 November 2005. Figure 11 shows sample acoustic slices taken over a 5 *m* radius across the river (left panel) and along the river (right panel). In 4 *m* of water, the images show 1.5-2 *m* of deposition upstream of the pier, with maximum deposition right at the piling. Interestingly, these steady river flow observations with no apparent surface wave energy are in contrast to that observed by the steady flow numerical simulations and laboratory wave flume observations obtained under strong surface wave action. These results suggest that deposition and scour around bridge piles in riverine flow may be significantly altered by the presence of large debris (e.g. trees limbs) hitting the stagnation point on the upstream side of the pier.

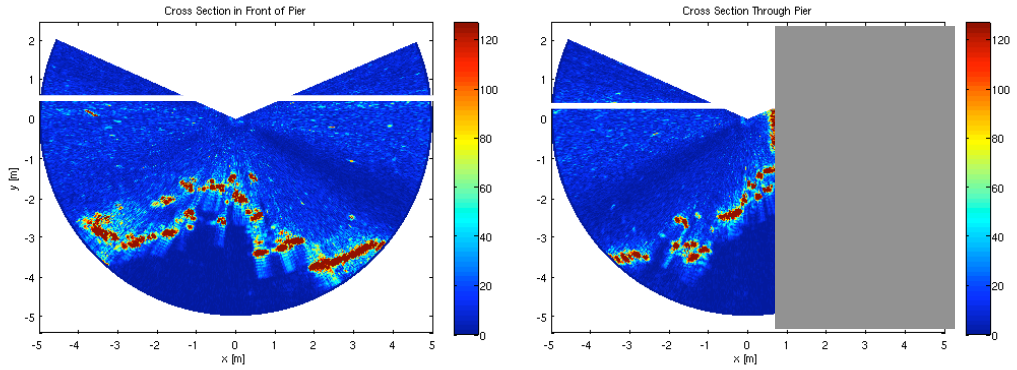

Figure 11. The 5 *m* radius cross sections of local bathymetry obtained in front of and perpendicular to the pier (left) and upstream of and in line with the pier (right). The colors indicate backscatter intensity with hot colors showing the high return of the bottom and the cool colors showing the low return of the water column. The white bands indicate approximate position of the water surface. The gray rectangle indicates the approximate location of the bridge pier. These images show a 2 *m* high deposition present upstream of the bridge pier that is consistent with the waverunner surveys.

Significance

Thus far, we have simulated the response of the fine scale flow field and local morphology around submerged objects in both two- and three-dimensional environments. In the two-dimensional mode, the flow around fixed, scoured bed profiles is simulated and compared favorably with laboratory observations (Smith and Foster, 2005). These results show that the CFD model (FLOW-3D) well captures the complexities of flow very near the bed and around objects placed close to or on the seabed. In addition to clear applications to pipelines and buried or unburied objects on the sea bed, this work sets the groundwork for looking at flows around vertical piles and bridge piers relevant to the present research. In the three-dimensional mode, the flow and scour of sediment beneath a cylindrical object lying on an initially flat bed is simulated and compared with laboratory observations that show excellent agreement in mean flow characteristics (Smith and Foster, 2006). This work demonstrates the capabilities of the numerical model to accurately resolve fine scale flows near obstacles (vertically or horizontally oriented) impinging on bottom topography with arbitrary form and with unconsolidated sedimentary material.

Numerical model results for combined wave-current flow about a vertical pile are in qualitative agreement with prototype laboratory observations, suggesting that the model is well reproducing the essential flow characteristics and sediment transport. In contrast, *in situ* acoustic observations of river topography at a bridge pier located on the Great Miami River (Hamilton, OH), where wave motions are minimal and river flow is approximately uni-directional and steady, show a distinct region of deposition just upstream of one of the pier pilings. This qualitative result suggests that deposition and scour around bridge piers in natural rivers can be significantly altered by the presence of large debris.

Future research efforts will utilize *in situ* acoustic observations of the river bed topography evolution, and surface remote sensing techniques to measure the surface flow fields, to initialize and verify the numerical model (verified with laboratory observations) to predict bed changes under a variety of flow conditions.

References

Chopakatla, S. C., T. C. Lippmann, and J. E. Richardson, 2008, Field verification of a CFD model for wave transformation and breaking in the surf zone, *J. Waterw. Port Coast. Ocean Eng.*, 134(2), 71-80.

FLOW-3D user's manual, 2002, *Flow Science, Inc*., Sante Fe, NM.

Hatton, K.A., D. L. Foster, P. A. Traykovski, P.A., and H. D. Smith, 2008, Scour and Burial of Submerged Mines in Wave Conditions, *IEEE-Journal of Ocean Eng.*, in press.

Hirt, C. W., and B. D. Nichols, 1981, Volume of fluid (VOF) method for the dynamics of free boundaries, *J. Comp. Phys.*, 39, 201-225.

Smith, H. D., and D. L. Foster, D.L., 2005, Modeling the Flow around a Cylinder above Scoured Bed, *ASCE J. Waterw., Port, Coastal and Ocean Eng.*, 131(1), 14-24.

Smith, H. D., and D. L. Foster, D.L., 2006, Three-dimensional flow around a bottom mounted short cylinder, *ASCE Journal of Hydraulic Engineering*, in press.

Testik, F. Y., Voropayev, S. I., and Fernando, H. J. S., 2005, Flow around a short horizontal bottom cylinder under steady and oscillatory flows. *Physics of Fluids*.

Publications resulting from this work

Hatton, K.A., D. L. Foster, P. A. Traykovski, P.A., and H. D. Smith, 2008, Scour and Burial of Submerged Mines in Wave Conditions, *IEEE-Journal of Ocean Engineering*, in press.

Smith, H. D., and D. L. Foster, D.L., 2005, Modeling the Flow around a Cylinder above Scoured Bed, *ASCE Journal of Waterway, Port, Coastal and Ocean Engineering*, 131(1), 14-24.

Abstracts of Work Presented at National and International Meetings

Hatton, K. A., and D. L. Foster, 2004, Scour and Burial of Submerged Mines in Wave Conditions, *Eos Trans. AGU*, 85(47), Ocean Sci. Meet. Suppl., Abstract OS21B-1222.

Foster, D. L., H. D. Smith, and K. H. Hatton, 2004, Modeling the 3-D Flow around a cylinder, *Mine Burial Workshop,* Woods Hole Oceanographic Institution, MA.

Nanoscale Modification and Functionalization of Carbon Electrodes for the Detection of Harmful Organic Chemicals in Water such as Phenol and Domoic Acid

Basic Information

Title:	Nanoscale Modification and Functionalization of Carbon Electrodes for the Detection of Harmful Organic Chemicals in Water such as Phenol and Domoic Acid
Project Number:	2007OH49B
Start Date:	9/1/2007
End Date:	8/31/2008
Funding Source:	104B
Congressional District:	1,2
Research Category:	Engineering
Focus Category:	Water Quality, Water Supply, Toxic Substances
Descriptors:	None
Principal Investigators:	Dionysios Dionysiou, Suzanne Lunsford

Publication

1. Yongjun Chen, 2007, PhD Dissertation, The Role of Preparation Conditions in Sol-Gel Methods on the Synthesis of Nanostructured Photocatalytic Films for Water Treatment, University of Cinncinatti.
2. Yongjun Chen, Suzanne Lunsford, and Dionysios D. Dionysiou, Photocatalytic Activity and Electrochemical Sensor Response of TiO2 Film with Macro/Mesoporous Texture, Thin Solid Films, accepted for publication.
3. Yongjun Chen, Suzanne Lunsford, and Dionysios D. Dionysiou. Sol gel synthesis of ZrO2 film modified carbon electrode for the detection of catechol (in preparation).
4. Yongjun Chen, Suzanne Lunsford, and Dionysios D. Dionysiou, Mesoporous ZrO2 film modified carbon electrode for the detection of Dopamine (in preparation)
5. Suzanne K. Lunsford, Amber Yeary, Jelynn Stinson, Hyeok Choi, and Dionysios D. Dionysiou, Electrochemical Analysis of Sonogel-Carbon Electrode Modified with Titanium Oxide (TiO2) to Detect Catecholamines in the Presence of Common Interferents. Proceedings of the General Papers Session, Division of Environmental Chemistry, Vol. 47, No.2, 234th American Chemical Society (ACS) National Meeting, August 19-23, 2007, Boston, Massachusetts.

Nanoscale Modification and Functionalization of Carbon Electrodes for the Detection of Harmful Organic Chemicals in Water

(Water Resources Center Annual Technical Report FY 2007)

Title:	**Nanoscale Modification and Functionalization of Carbon Electrodes for the Detection of Harmful Organic Chemicals in Water**
Project Number:	
Start Date:	March 1, 2007
End Date	February 28, 2008
Funding Source	104B
Congressional District:	1
Research Category:	Engineering
Focus Category:	Water Quality (WQ); Water Supply (WS); Toxic Substances (TS)
Descriptors:	None
Principal Investigators:	Dionysios (Dion) D. Dionysiou, Suzanne K. Lunsford

TITLE: Nanoscale Modification and Functionalization of Carbon Electrodes for the Detection of Harmful Organic Chemicals in Water

PI : Dionysios (Dion) D. Dionysiou, Ph.D.
Associate Professor
Department of Civil and Environmental Engineering
University of Cincinnati, Cincinnati, OH
Co-PI: Suzanne K. Lunsford, Ph.D.
Associate Professor
Department of Chemistry
Wright State University, Dayton, OH
Research Team: Yongjun Chen (Ph.D./Postdoctoral Fellow)
START DATE: March 1, 2007
END DATE: February 28, 2008

Summary of the work

The study is mainly focused on (1) fundamental understanding on the relationship of microstructure of metal oxide films to electrochemical sensors, and (2) the development of new metal oxide materials, which have great potential in the application of electrode materials. In the part A of this study, we deal with the synthesis of thick anatase TiO_2 films with macro-mesoporous structure. Such a pore structure is beneficial to the improvement in mass transfer between the treated contaminants and active sites in the inner layers of such thick films. Among different types of polyethylene glycol (PEG), used as template, with different molecular weight, PEG 2000 was found as the most suitable template for improving the texture of these TiO_2 films. The results show that after optimizing the PEG 2000 loading in the sol, macro-mesoporous TiO_2 films are obtained which possess enhanced electrochemical response and good mechanical stability. The content of this part has been published in Thin Solid Films (in press). In part B of this study, we employed sol gel method to prepare sonogel carbon electrode modified by ZrO_2 film. A systematic investigation on the relationship of the properties of electrode materials with the electrochemical response to the neurotransmitters (i.e., catechol and dopamine) was performed. It was found that sol gel derived ZrO_2 film was a promising inorganic material on the application of electrochemical sensors to detect neurotransmitters. On the third part, we developed a novel sol gel route to synthesize mesoporous ZrO_2 film (M-ZrO_2 film), which is associated with the use of nonionic surfactant Tween 20 as template through a self-assembly pathway. It was found that sonogel carbon electrode modified by this type of M-ZrO_2 film possesses high sensitivity and stability in the detection of neurotransmitters.

Problem and Research Objectives

Recently, new advances in environmental health are revealing that anthropogenic or naturally occurring harmful organic chemicals in sources of water supply expose a great health threat to human and aquatic life. Due to their well-known carcinogenic and lethal properties, the presence of human-produced toxic chemicals such as phenol and its derivatives poses a critical threat to human health and aquatic life in such water resources of the state of Ohio. Currently, there is an urgent need to develop more innovative and effective *in-situ* measurement methods to detect target toxins of interest in water, and thus assess their environmental fate and distribution in water bodies and ecosystems. In order to achieve effective assessment and monitoring of the toxins, the preliminary requirement is to detect them quickly in subseconds with a more efficient, innovative, and *in-situ* method. Electrochemical detection of target compounds of interest using smart sensors has attracted more attention for analytical chemists due to its simplicity, rapidness and high sensitivity. However, considering the real challenges in achieving successful analysis of chemicals in the presence of common interferents in water resources, the properties of the electrode should be significantly improved before the electrode can become competitive for full-scale applications in developing such sensors to detect toxic chemicals in water. Recently, a sonogel carbon electrode modified by nanostructured TiO_2 films, a new class of sensor, had been successfully developed in our group, which is associated with employing sol gel technology to coat TiO_2 film on the top of sonogel graphite carbon electrode. The modified electrode had been proved to be promising sensor to detect neurotransmitters, such as catechol and dopamine. Since there are many challenging requirements to guarantee safety, reproducibility and reliability in the application of sensors, including sensitivity, selectivity and stability, it is necessary to further optimize our fabrication technology.

Initially, this work was associated with the synthesis of carbon electrodes modified by metal oxides including TiO_2, TiO_2-ZrO_2 or ZrO_2 to detect toxic chemicals in water such as phenol. Preliminary data indicated that there was electrochemical response to phenol in neutral pH aqueous solution using carbon electrode modified by ZrO_2 metal oxide particles. However, there were still certain challenges that needed to be overcome related to sensor sensitivity, selectivity and stability. Therefore, the project objectives were adjusted and mainly fused on the fundamental understanding on the relationship of microstructure of metal oxides to their electrochemical responses. This was a necessary and important procedure for developing accurate and smart nanostructured electrodes to detect phenol and domoic acid. In order to make a comparative study between our new methods and former studies, we perform evaluation of the as-prepared electrodes using catechol and dopamine, which were previously used in our laboratories.

Research objectives: The main objectives of the study were to (1) obtain mechanistic understanding on the relationship of structure properties of metal oxides to their electrochemical response, and (2) explore new metal oxides as effective electrode materials.

Part A: Photocatalytic activity and electrochemical response of Titania films with macro/mesoporous texture

A.1 Abstract

Multifunctional anatase titania (TiO_2) films with macro/mesoporous texture were prepared using a non-acidic polyethylene glycol-associated titanium alkoxide precursor sol, followed by 500 ^oC calcination. It was found that increasing polyethylene glycol 2000 loading in the sol not only increases the macroporous size in the films, but can also lead to an enhancement of mesopore volume (the number of mesopores). This is considered to have major contribution to increasing the final specific surface area due to inhibition of pore shrinkage or collapse at high calcination temperature (i.e., 500 ^oC). Good dissolution of polyethylene glycol 2000/acetonitrile solution in the isopropanol based sol can lead to the formation of the resulting TiO_2 films with uniform and macroporous surface morphology. The film at optimum polyethylene glycol loading (20 g/L polyethylene glycol 2000, 500 ^oC) exhibits good mechanical stability, enhanced photocatalytic activity in the degradation of 2, 4-dichlorophenol in water and superior electrochemical response to catechol in the presence of ascorbic acid (a common interferent) by cyclic voltammetry. The unique textural structure, including enhanced specific surface area /pore volume and macroporous morphology with mesoporous anatase titania wall (average macrospore size in the range of 150-200 nm, mesoporous size of ~5 nm) are considered to be the main factor attributing to such a multifunction of the titania films.

A.2 Introduction

Development of porous TiO_2 films is becoming an important topic for a variety of applications such as environmental remediation [1-13], sensors [13-15], and dye-sensitized solar cells [13, 16-18]. Currently, polyethylene glycol (i.e., PEG, in variety of molecular weights) is considered as a popular and effective polymer template for the formation of macroporous TiO_2 thin films, which can be utilized for the purification of air and water because of their unique structure (i.e., high Brunauer–Emmet–Teller (BET) specific surface area and macroporous morphology) [6-12]. Recently, it has been reported that crack free TiO_2 films with hierarchical macro/mesopore texture can be formed from a PEG associated acidic titanium alkoxide precursor sol by adjusting processing conditions [19]. However, such a macro/mesoporous texture of TiO_2 films induced by decomposing PEG from a basic titanium alkoxide precursor sol has not yet been reported in detail. Specifically, pH is an important parameter to affect texture properties of the sol-gel derived TiO_2 photocatalysts [19, 20] and a basic precursor sol (i.e. PEG-Diethanolamine (DEA)-associated sol) is beneficial to avoid acidic corrosion on metal substrate, in particular, stainless steel, during calcination. In this study, a basic PEG-associated titanium alkoxide sol is employed to investigate the effect of PEG loading on the adhesion, surface morphology, and texture in inorganic wall of TiO_2 films coated on stainless steel substrate. The photocatalytic activities of such films in the degradation of 2, 4-dichlorophenol (2, 4-DCP), a toxic chlorinated organic compound in water, are evaluated. In addition, based on a former report that porous anatase TiO_2 films are suitable materials for the application of

electrochemical sensor in the detection of catechol, a type of neurotransmitter [15], another purpose of this study is to examine the electrochemical sensor performance of these TiO_2 films coated on carbon electrodes for the detection of neurotransmitters such as catechol and dopamine by utilizing cyclic voltammetry.

A.3 Experimental details

A.3.1 Synthesis of TiO_2 films

Titanium tetraisopropoxide (TTIP, 97%, Aldrich,), isopropanol (99.9%, Fisher Scientific), and diethanolamine (99%, Fisher Scientific) were used for the preparation of the conventional titania sol. Polyethylene glycol with molecular weight of 400, 1000, and 2000 (Aldrich) was used as template agent for macropore formation. Acetonitrile (99.5%, Aldrich) was used as solvent to dissolve polyethylene glycol 1000 (PEG 1000) and polyethylene glycol 2000 (PEG 2000). 304 stainless steel was used as the substrate to support the photocatalytic films. The preparation procedure for making titania sol (without PEG) is similar to that reported in former publications [21, 22]. In this study, we employed DEA with DEA/TTIP molar ratio of 1:1. Polyethylene glycol with molecular weight of 400 (PEG 400) was directly added into the titania sol to make the modified sol. PEG 1000 and PEG 2000 solutions were prepared using 0.3 g PEG /mL-acetonitrile. PEG/acetonitrile solutions were dissolved into the titania sol immediately without any precipitation. A dip-coating apparatus was used for dipping in and pulling out the coated stainless steel from the as-prepared sols. The dip coating velocity was kept constant at 12.3±0.5 cm min^{-1}. The materials and method to prepare sonogel carbon (SGC) electrode is the same as that in a former study [15], except a 0.5 mm copper wire (Alfa Aesar) was employed. The TiO_2 gel can be coated on the tip of SGC electrodes by dipping the tip of carbon electrode into the sol and taken out. The relative humidity and room temperature in the lab were ~50% and 23 ^oC, respectively. After the sols had been coated on the stainless steel substrate or the tip of carbon electrodes, the coated stainless steel or coated carbon electrodes were calcined in a programmable high temperature furnace. The furnace temperature was incremented at a ramp rate of 3.0 °C min^{-1} until 100°C; this temperature was held for 1 hour. The temperature of the oven was subsequently increased at a ramp rate of 3.0 °C min^{-1} to 500 ^oC and was held at this value for one hour. Finally, the films were cooled naturally to room temperature.

A.3.2 Characterization of TiO_2 films

The crystal phase composition of the TiO_2 films coated on stainless steel was determined by X-ray diffraction (XRD) using a Siemens Kristalloflex D500 diffractometer with Cu Kα radiation. Film morphology and film thickness on the stainless steel substrate were characterized by an environmental scanning electron microscope (ESEM, Philips XL 30 ESEM-FEG) with accelerating voltage of 10 K. To prepare and mount the film for cross-section scanning electron microscope (SEM) analysis, the transoptic mounting powder (Mark V Laboratory) together with a small coated stainless steel coupon were poured into a circular mold and heated for 15 min, then cooled down for 15 min. After the mounted coating was taken out of the mold, the top surface of

the resin with inserted coating was polished using sandpaper fixed to a rotating polishing disk. The bottom surface of the acrylic cylinder together with the bottom edge of the coated coupons were sequentially polished by sandpapers with Grit numbers of 240, 320, 400, 600, 800 and 1200. After finishing this procedure, the mounted coating was analyzed by cross section SEM. It should be noted that no charge fluorescent effect was observed during SEM analysis for the samples. The crystal and pore morphology of the films were determined by a JEM-2010F (JEOL) High Resolution-Transmission Electron Microscope (HR-TEM) with field emission gun at 200 kV. All powder samples were obtained by scrapping from the coating on the stainless steel and dispersed in methanol (High Performance Liquid Chromatography (HPLC) grade, Pharmco) using an ultrasonic cleaner (2510R-DH, Bransonic) for 5 min and fixed on a carbon-coated copper grid (LC200-Cu, EMS).

The specific surface area and pore volume of the films were measured using a Micromeritics TriStar 3000 Gas Adsorption Analyzer. All powder samples were obtained by scraping from the coating on the stainless steel substrate and were purged with nitrogen gas for 3 h at 150 ^{o}C before N_2 adsorption–desorption isotherm analysis. The strength of adhesion of the TiO_2 films on stainless steel substrate was measured by the cross hatch adhesion test (ASTM D3359B-02 [23]). The cut samples were also examined by a microscope (The Buehler VersaMet®3 metallograph, U.S.A).

A.3.3 Photocatalytic activity evaluation of TiO_2 films

The photocatalytic activity of the TiO_2 films was evaluated using 2, 4-DCP aqueous solution with an initial concentration of approximately 18 mg/L. The solution volume was 20 ml with initial pH 5.8. The photocatalytic reactor used was a round cell with inside dimensions of 9 cm. The dimensions of the coated stainless steel were 5.7 cm (length) by 5.1 cm (width). The UV source consisted of two 15 W integrally filtered low-pressure mercury UV tubes (Spectronics Corp., Westbury, New York) emitting radiation with wavelength in the range 300-400 nm and a peak at 365 nm. The average intensity of the UV radiation for each tube was approximately 72.8 $\mu W/cm^2$ measured by a UV radiation meter (IL 1700 International Light, Serial No. 2547) at a distance of 16.5 cm from the center of the tube to the bottom of the reactor. The tubes were mounted in pairs in two silver-anodized housings positioned vertically on the top of the reactor at a distance of 16.5 cm. A fan (Duracraft Corporation, South Borough, Massachusetts) was used to avoid significant enhancement of temperature in reaction solution. The concentration of the 2,4-DCP in the reactor was analyzed using HPLC (Agilent 1100 series) equipped with a QuatPump, a UV–vis diode array detector and an autosampler. The column used for the analysis was an Eclipse XDB-C8 column obtained from Agilent and the mobile phase was H_2SO_4 (70% v/v, 0.01 N) and acetonitrile (30% v/v, HPLC grade).

A.3.4 Electrochemical sensor response

Electrochemical sensor response to catechol or dopamine was carried out using an Electrochemical Workstation (Epsilon, Bioanalytical Systems) based on Cyclic voltammetry (CV) with three

electrode compartment cell. The electrochemical compartment cell was composed of a Pt auxiliary electrode (Bioanalytical Systems), Ag/AgCl reference electrode (Bioanalytical Systems), and the modified working TiO_2/SGC electrode. 5 mM catechol ($C_6H_4(OH)_2$, Fluka) solution or 5 mM dopamine ($C_8H_{11}NO_2HCL$, Aldrich) solution was prepared in 0.1 M sulfuric acid (Aldrich) with deionized water, while 5 mM catechol solution mixed with 5 mM ascorbic acid ($C_6H_8O_6$, Aldrich), a common interferent, was prepared in 0.1 M sulfuric acid (Aldrich) with deionized water. The scan rate of CV was 100 mV s^{-1}.

A.4 Results and discussion

The results of BET surface area and pore volume of TiO_2 films at different PEG types and loadings are presented in Table 1. It can be seen that, the BET surface area and pore volume can be improved at different extent by increasing PEG loading. Among PEG series chosen, PEG 2000 was the most effective template for the improvement in BET surface area and pore volume of the films. Therefore, in the following part of this paper, we are focused on studying TiO_2 films prepared with different PEG 2000 loading in the isopropanol-associated titanium alkoxide sol.

Table 1. BET surface area and total pore volume of TiO_2 films prepared with PEG of different molecular weight and at different loading in the sol.

TiO_2 film	PEG molecular weight	PEG loading in the sol (g/L)	BET (m^2/g)	Pore volume (cm^3/g)*
Conventional TiO_2 film	-	0	11.2	0.0191
TiO_2 –PEG film	PEG 400	15	11.4	0.0200
TiO_2 –PEG film	PEG 1000	15	13.1	0.0206
TiO_2 –PEG film	PEG 2000	15	17.3	0.0410
TiO_2 –PEG film	PEG 400	20	16.4	0.0259
TiO_2 –PEG film	PEG 1000	20	14.2	0.0204
TiO_2 –PEG film	PEG 2000	20	26.6	0.0670

* BJH Adsorption cumulative volume of pores.

It has been well established that decomposing PEG in the films can create macropores in the TiO_2 film formed from the PEG ethanol-associated sol-gel procedure [24-27]. The mechanism of macropore formation is related to solvent volatilization and phase separation between PEG and solvent during the period of drying and calcination [24]. The higher the amount of PEG is the larger is the pore size [9, 25-27]. To assess how PEG 2000 loading in the isopropanol-associated titania sol affected the surface morphologies of TiO_2 films, SEM analysis of the films (2 dip coating layers) was performed and the images are shown in Fig. 1.

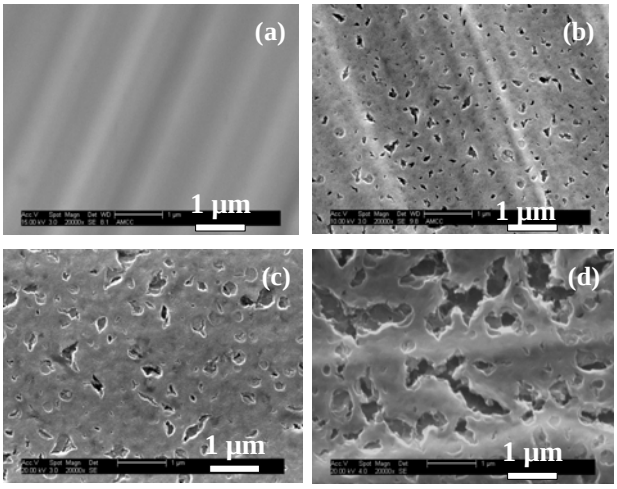

Fig. 1. SEM images of the TiO_2 films (a) no PEG addition, (b) 15 g/L PEG 2000, (c) 20 g/L PEG 2000, and (d) 25 g/L PEG 2000.

It can be seen that the TiO_2 film fabricated from the coated gel without PEG addition (Fig. 1a) exhibits a "smooth", crack free and non-porous morphology, while the surface of the TiO_2 films with PEG addition in the sol is full of macropores. Increasing PEG 2000 loading from 15 to 25 g/L leads to an enhancement of the macroporous size. The average macropore size reaches 100-150, 150-200, and above 200 nm for TiO_2 film with PEG 2000 loading of 15, 20, and 25 g/L, respectively (refer to Table 2).

Table 2. Crystal size, pore size, BET surface area and total pore volume of TiO_2 films prepared at different loading of PEG 2000 in the sol.

PEG 2000 (g/L)	Crystallinity	Crystal size[a] (nm)	BET (m^2/g)	Pore volume[b] (cm^3/g)	Average macropore size[c] (nm)	Mesoporous size at highest pore volume[d] (nm)
0	Anatase	22	11.2	0.0191	-	6.2
15	Anatase	19	17.3	0.0410	100-150	6.2
20	Anatase	16	26.6	0.0670	150-200	5.3
25	Anatase	14	38.4	0.0442	Above 200	3.8

[a] Based on XRD, using Scherrer equation: $D=0.9\times\lambda/(B\times\cos\theta)$, where $\lambda=0.154$ nm.

[b] BJH Adsorption cumulative volume of pores.

[c] Based on SEM.

[d] BJH adsorption pore size with highest pore volume.

Meanwhile, it should be noticed that, increase in the PEG loading cannot cause crack formation until the PEG loading reaches 25 g/L. Such "crack" is in fact the interconnected macropores, which may have a detrimental effect on the long-term mechanical stability of the films in applications for water treatment. Considering that adhesion is an important property for immobilized photocatalytic film in such water treatment applications, all films were examined by the cross hatch tape test. The results are presented in Table 3.

Table 3. Adhesion of TiO_2 films prepared at different loadings of PEG 2000 in the sol. (Two dip coating layers on the stainless steel substrate, 500°C calcination).

PEG 2000 (g/L)	0	10	15	20	25
Rank*	5 B Excellent	5 B Excellent	5 B Excellent	4-5B Good-Excellent	3 B Fair

* ASTM D3359B-02 [23].

It was found that the adhesion decreases from 4-5B to 3B as the PEG 2000 loading increases from 20 g/L to 25 g/L. The decreased adhesion may be attributed to the decreased mechanical strength induced by the formation of the interconnected macropores. Therefore, 20 g/L PEG 2000 is the maximum loading for obtaining good structural integrity and excellent adhesion between the TiO_2 film and the stainless steel substrate.

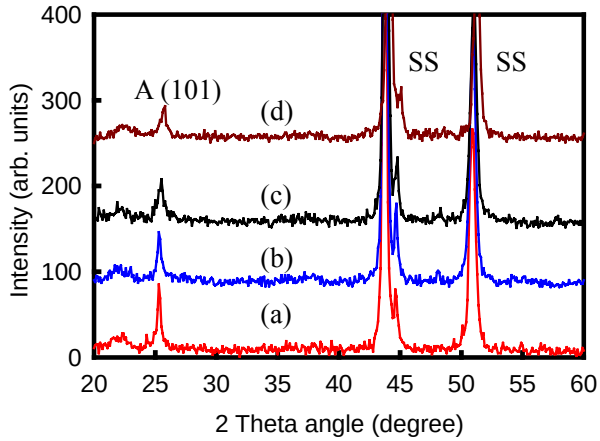

Fig. 2. XRD spectra of TiO_2 films: (a) conventional film, (b) 15 g/L PEG 2000, (c) 20 g/L PEG 2000, and (d) 25 g/L PEG 2000 (2 dip coating layers, 500°C calcination, stainless steel substrate).

Fig. 2 shows the results of the crystal structure of TiO_2 films prepared at different PEG 2000 loadings in the sol. All films exhibit a peak at 2 theta angle of approximately 25.4 degrees, which corresponds to the anatase phase (101). It can be observed that there is a slight increase in the full

peak width at half maximum intensity, which suggests the increasing PEG 2000 loading could cause a decrease in the crystal size of the films. In order to check if the coated films have been better crystallized and to obtain information on the interparticle pore shape, these films were also examined by HR-TEM with Selected Area Diffraction (SAD). The results showed that all films had been well crystallized.

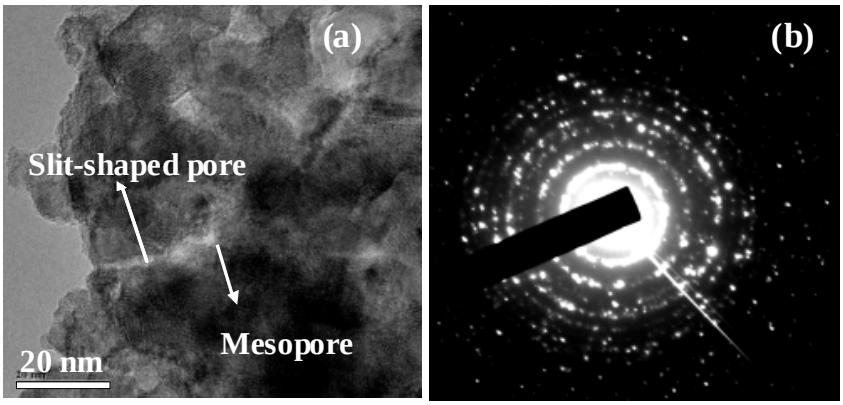

Fig. 3. HR-TEM image (a) and Selected Area Diffraction pattern (b) of TiO_2 film with 20 g/L PEG 2000.

As an example, Fig. 3 shows a HR-TEM image of TiO_2 film with 20 g/L PEG 2000. Larger slit-shaped pores and small mesopores (Fig. 3(a)) among the particles with lattice fringes can be observed and there is no obvious diffusion ring in the SAD image (Fig. 3 (b)). Based on the above discussion on the results of XRD, it can be concluded that all TiO_2 films have mesoporous anatase wall. In addition, considering the fact that (i) the TiO_2 film with 20 g/L PEG 2000 has large porosity, and (ii) the presence of a notable peak at 2 theta angle of 25.4 degrees for the film with only 2 dip coating layers, we expected the film thickness of TiO_2 film with 20 g/L PEG 2000 to be large. The film thickness of TiO_2 film with 20 g/L PEG 2000 was measured by cross-section SEM and the images are shown in Fig. 4.

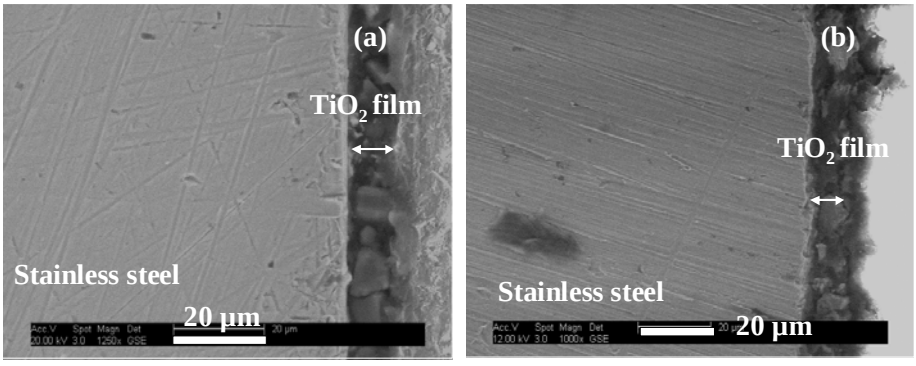

Fig. 4. Cross-section SEM image of TiO_2 film. (a) 2 dip coating layers, and (b) 4 dip coating layers.

The results show that the film thickness is large, reaching approximately 3 μm (1 dip coating layer). It has been reported that PEG had some positive effects on the film thickness [28]. Therefore, formation of such thick films may be correlated to several factors, including isopropanol solvent, PEG 2000 and the stainless steel substrate.

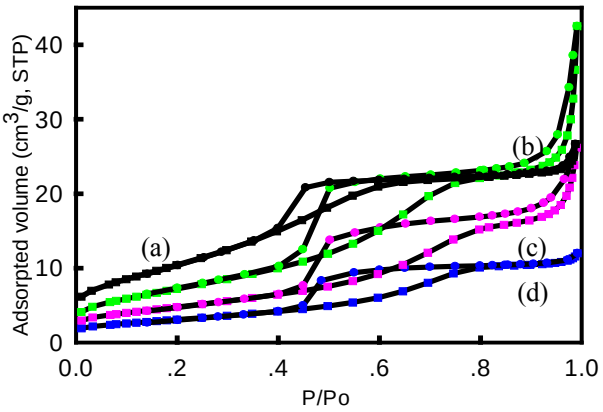

Fig. 5. Nitrogen adsorption and desorption isotherms of TiO_2 films prepared at: (a) 25 g/L PEG 2000, (b) 20 g/L PEG 2000, (c) 15 g/L PEG 2000, and (d) conventional TiO_2 film (no PEG added).

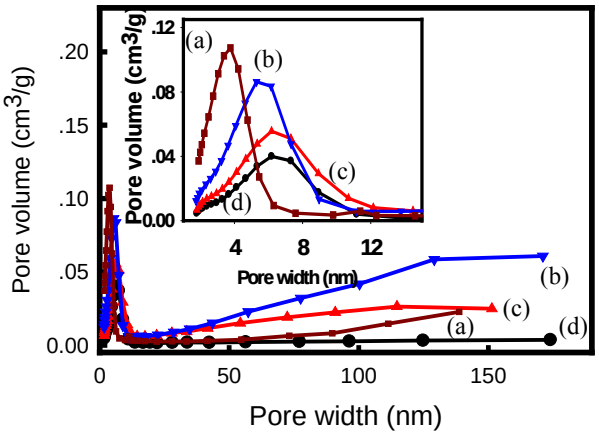

Fig. 6. Pore size distribution curves of TiO_2 films prepared at different PEG loadings.
(a) 25 g/L PEG 2000, (b) 20 g/L PEG 2000, (c) 15 g/L PEG 2000, and (d) no PEG addition.

Figs. 5 and 6 show respectively (i) nitrogen adsorption and desorption isotherms, and (ii) pore size distribution of TiO_2 films prepared at different PEG 2000 loading. From Fig. 5, it can be seen that all samples are of type IV (IUPAC classification). The hysteresis loop of TiO_2 film without PEG 2000 addition only shows type H2, while the hysteresis loop of TiO_2 films with PEG 2000 loading of 15 g/L and 20 g/L in the sol shows type H2 at relatively lower pressure range and type H3 at relatively

higher pressure range. Because some slit-shaped large pores can be observed in these films (refer to Fig. 3(a)), the type H3 at higher pressure range is believed to be due to the formation of slit-shaped large pores, which is most probably induced by decomposing PEG 2000. As the PEG 2000 loading reaches 25 g/L in the sol, the hysteresis loop of TiO_2 film exhibit a type of near H2 (refer to adsorption isotherm (a)). This is due to the fact that many macropores have transformed into interconnected open large pores ("crack"), which can not induce capillary condensation during the N_2 adsorption-desorption process. Table 2 lists the results of BET surface area and total pore volume of TiO_2 films synthesized at different PEG 2000 loadings in the sol. It can be observed that the BET surface area and total pore volume increase as the PEG 2000 loading increases from 10 g/L to 20 g/L. However, as the PEG 2000 loading reaches to 25 g/L, although the BET surface area increases, the total pore volume decreases. This is due to the fact that macropores also contributed to the total pore volume. Results in Fig. 6 show that increasing the PEG 2000 loading from 0 to 20 g/L in the sol, can obviously increase the volume of small pores (i.e., mesopores) and macropores. From the inserted graph in Fig. 6, it can be more clearly seen that increasing PEG loading lead to decreased size of mesopores and enhanced volume of mesopores, which demonstrate that increasing PEG loading not only inhibits crystal growth at some extent, but also inhibits small pore shrinkage or collapse induced by crystal sintering under high calcination temperature (i.e., 500°C). Therefore, enhanced BET surface area is mainly attributed to the enhanced volume of small pores or the number of small pores (i.e., mesopores).

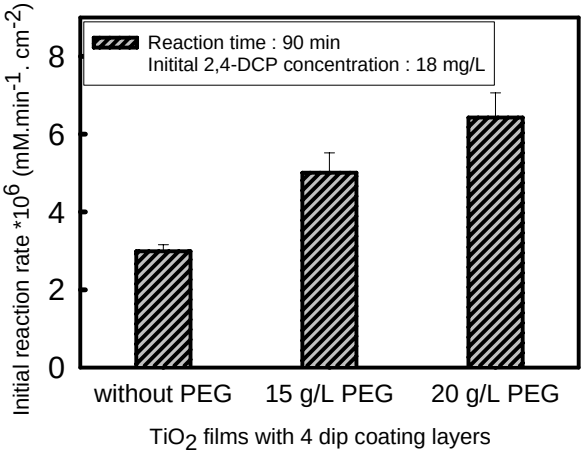

Fig. 7. Photocatalytic degradation of 2,4-DCP contaminant in water.
Conditions of the photocatalytic experiments: UV 300-400 nm (peak at 360 nm), 2,4-DCP solution at pH=5.8 and initial concentration of 18 mg/L. Films prepared at different PEG 2000 loading (4 dip coating layers on the stainless steel substrate, 500°C).

Fig. 7 shows the results of the photocatalytic degradation of 2,4-DCP, a model organic contaminant, using TiO_2 films with different loadings of PEG 2000. Control tests (no UV radiation or only UV radiation without TiO_2 films) show that there is no obvious volatilization or degradation of 2,4-DCP within 90 min. Therefore, the degradation of 2,4-DCP in Fig. 7 is attributed to the photocatalytic

reaction of TiO_2 films. The results clearly show that increasing PEG loading leads to an enhancement in photocatalytic activity of TiO_2 films. This can be explained by the increase in surface area and pore volume. When PEG 2000 loading reaches 20 g/L, the initial reaction rate of photocatalytic degradation 2,4-DCP in macroporous TiO_2 film can reach 6.43 $\times 10^{-6}$ mM min^{-1} cm^{-2}, which is above two times that of TiO_2 film without PEG. Considering that the macroporous TiO_2 film with 20 g/L PEG 2000 has the highest photocatalytic activity and good mechanical properties, this type of thick film is considered to be a promising photocatalyst suitable for the destruction of organic contaminants in water, especially under conditions of low corrosivity.

The concept of electrode modification originated over three decades ago with work of several research groups. Considering this fact, our research group has developed a titanium dioxide modified carbon electrode to be a promising electrochemical sensor for the detection of catecholamines, a class of neurotransmitters in the neuroscience field [15]. In this study, the modified TiO_2 films are coated on the tip of sonogel carbon electrode, in order to evaluate their electrochemical response for the detection of catechol in the presence of ascorbic acid, a common interferent.

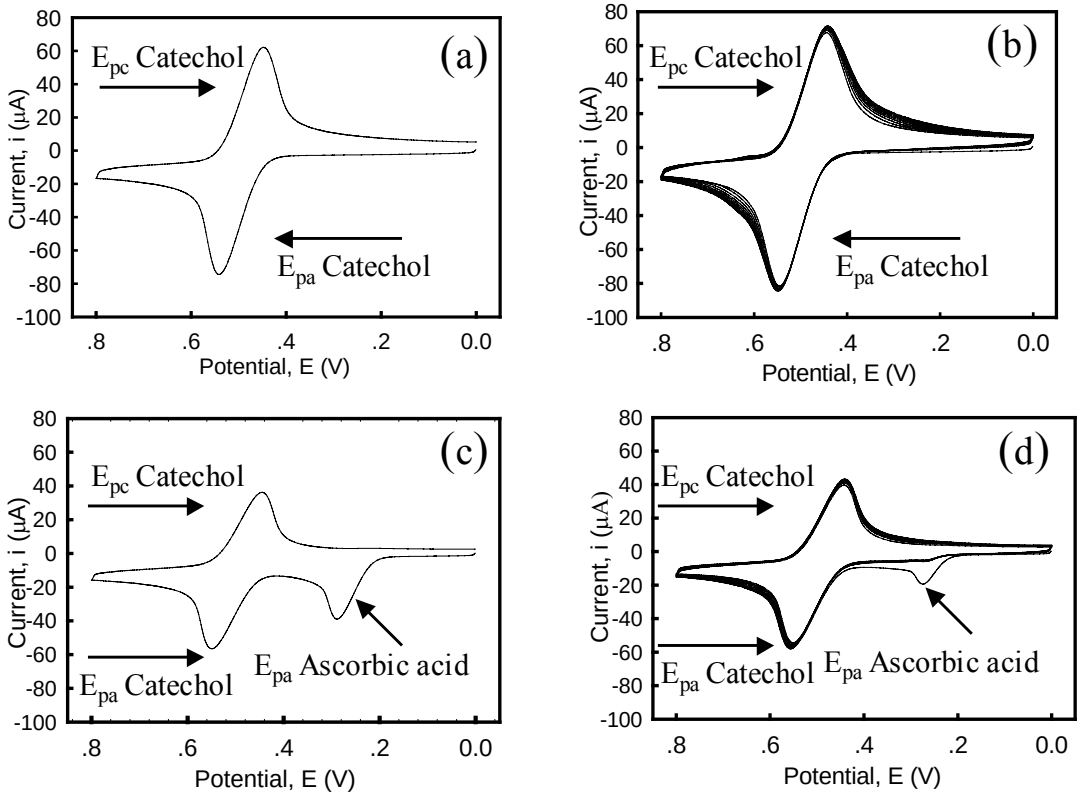

Fig. 8. Cyclic voltammograms of sonogel carbon electrode (a) 5 mM catechol , 2 scans; (b) 5 mM catechol, 20 scans; (c) 5 mM catechol in the presence of 5mM ascorbic acid, 2 scans; (d) 5 mM catechol in the presence of 5mM ascorbic acid, 20 scans; scan rate 100mV/s, electrolyte 0.1 M sulfuric acid.

Fig. 8 (a), (b), (c), and (d) illustrate the electrochemical response of the sonogel carbon electrode modified by the TiO_2 film with 20g/L PEG 2000 loading on the detection of catechol. It can be clearly observed that there is an enhanced electrochemical response to catechol in the presence of ascorbic acid, including improved reversible behavior of catechol and improved irreversible behavior of ascorbic acid. From Fig. 8(b) and (d), it can be concluded that such a TiO_2 modified carbon electrode can exhibit less edge effect, excellent stability, and reproducibility for the detection of catechol, even in the presence of ascorbic acid (a common interferent). It has been well established that formation of macropore channels in catalysts is beneficial to facilitate mass transfer of the chemicals to the active sites and that improvement in mesopore (or micropore) structure is beneficial to the enhancement in the BET surface area [29,30]. As a result, the enhancement in macro/mesoporous textural structure of the film is beneficial to the acceleration of mass transfer of the chemicals to the catalyst active sites and the formation of large number of active sites to absorb chemicals to the surface of the catalyst [3, 29]. Therefore, such good electrochemical responses are believed to be associated to such a macro/mesoporous texture of the film.

Moreover, such a kind of titanium dioxide modified carbon electrode has also been found to present a good electrochemical response to dopamine (5 mM) in acidic solution (figures are not shown in the text), which is another type of neurotransmitter in the neuroscience field [15]. Therefore, the as-prepared electrode has a great potential to detect other types of neurotransmitters. It should be emphasized that, sensor response time, another important performance characteristic of the sensor, can be affected by mass transfer of the chemical molecules to the surface of the electrodes [31]. The formation of macrospores in the film is believed to be beneficial to short sensor response time, which has been observed in our experiment (i.e., a few seconds). Consequently, it is worthy to further investigate some important aspects associated with the sensor application of such a macro/mesoporous TiO_2 film, including its sensitivity, linearity under different concentrations of chemicals, and electrochemical response to other chemicals. Such research works are underway in our group.

A.5 Conclusions

A simple externally-added solvent (i.e., acetonitrile) PEG-associated sol gel method is developed to synthesize multifunctional anatase TiO_2 films with macro/mesoporous texture. Good dissolution of PEG 2000/acetonitrile in the isopropanol solvent lead to the formation of the final TiO_2 films with uniform and macroporous surface morphology. The films formed at optimum molecular weight of PEG and PEG loading (20 g/L, PEG 2000) exhibit some advantageous properties including enhanced BET surface area and pore volume, resistance in crack formation, good mechanical stability, enhanced photocatalytic activity in the degradation of 2,4-dichlorophenol and good electrochemical sensor response to catechol, even in the presence of ascorbic acid. The enhanced BET surface area induced by decomposing PEG 2000 is mainly attributed to the enhanced volume of small pores (i.e., mesopores) in the films.

A.6 References

[1] J. C. Yu, L. Zhang, J. Yu, Chem. Mater. 14 (2002), p. 4647.

[2] J. C. Yu, J. G. Yu, J. C. Zhao, Appl. Catal. B: Environ. 36 (2002), p. 31

[3] Y. J. Chen, D. D. Dionysiou, Appl. Catal. A: General. 317 (2007), p. 129.

[4] Y. J. Chen, E. Stathatos, D. D. Dionysiou, Sur. Coat. Technol. 202 (2008), p.1944.

[5] H. Choi, E. Stathatos and D. D. Dionysiou, Appl. Catal. B: Environ. 63 (2006), p. 60.

[6] G. Lei, M. H. Xu, J. Sol-Gel Sci. Technol. 43 (2007), p. 1.

[7] T. Kitamura, H. Kumazawa. Chem. Eng. Comm. 192 (2005), p. 795.

[8] B. Guo, Z. L. Liu, L. Hong, H. X. Jiang, J. Y. Lee, Thin Solid Films 479 (2005), p. 310.

[9] B. Guo, Z. l. Liu, L. Hong, H. X. Jiang. Surf. Coat. Technol. 198 (2005), p. 24.

[10] Y. Kotani, T. Matoda, A. Matsuda, T. Kogure, M. Tatsumisago, T. Minami, J. Mater. Chem. 11 (2001), p. 2045.

[11] J. G. Yu, X. J. Zhao, Q. N. Zhao, Thin Solid Films 379 (2000), p. 7.

[12] N. Nobuaki, T. Koji, I. Takashi, J. Sol-Gel Sci. Technol. 13 (1998), p. 691.

[13] X. B. Chen, S. S. Mao, Chem. Rev. 107 (2007), p. 2891.

[14] K. D. Benkstein, S. Semancik. Sens. Actuators, B, 113 (2006), p. 445.

[15] S. K. Lunsford, H. Choi, J. Stinson, A. Yeary, D. D. Dionysiou, Talanta, 73 (2007), p. 172.

[16] M. Okuya, K. Nakade, S. Kaneko, Sol. Energy Mater. Sol. Cells 70, (2002), p. 425.

[17] E. Stathatos, P. Lianos, J. Nanosci. Nanotechnol. 7 (2007), p. 555.

[18] E. Stathatos , P. Lianos, C. Tsakiroglou, Microporous Mesoporous Mater. 75 (2004), p. 255.

[19] M. C. Fuertes and G. J. A. A. Soler-Illia. Chem. Mater. 18 (2006) p. 2109.

[20] G. J. A. A. Soler-Illia, C. Sanchez, B. Lebeau, J. Patarin, Chem. Rev. 102 (2002), p. 4093.

[21] Y. Takahashi, Y. Matsuoka, J. Mater. Sci. 23 (1988), p. 2259.

[22] Y. J. Chen, D. D. Dionysiou, Appl. Catal. B: Environ. 69 (2006), p.24.

[23] American Society for Testing and Materials, ASTM, West Conshohocken, PA, D-3359-02 cross-cut tape test for adhesion.

[24] S. J. Bu, Z. G. Jin, X. X. Liu, L. R. Yang, Z. J. Cheng, J. Sol–Gel Sci. Technol. 30 (2004), p. 239.

[25] K. Kato, A. Tsuzuki, Y. Torii, H. Taoda, T. Kato, Y. Butsugan, J. Mater. Sci. 30 (1995), p.

837.

[26] J. G. Yu, X. I. Zhao, J. C. Du, W. M. Chen. J. Sol–Gel Sci. Technol. 17 (2000), p. 163.

[27] S. J. Bu, Z. G. Jin, X. X. Liu, L. R. Yang, Z. J. Cheng, J. Sol–Gel Sci. Technol. 30 (2004), p. 239.

[28] T. Miki, K. Nishizawa, K. Suzuki, K. Kato. J. Mater. Sci. 39 (2004), p. 699.

[29] X. C. Wang, J. C. Yu, C. M. Ho, Y.D. Hou, X. Z. Fu. Langmuir 21 (2005), p. 2552.

[30] Y. Zhang, M. Koike, N. Tsubaki. Catal. Letters. 91 (2005), p.193.

[31] P. R. Warburton, M. P. Pagano, R. Hoover, M. Logman, K. Crytzer, Y. J. Warburton. Anal. Chem., 70 (1998), p. 998.

Evaluating Colloid Release from Natural and Model Porous Media

Basic Information

Title:	Evaluating Colloid Release from Natural and Model Porous Media
Project Number:	2007OH54B
Start Date:	10/1/2007
End Date:	9/30/2008
Funding Source:	104B
Congressional District:	15
Research Category:	Water Quality
Focus Category:	Solute Transport, Groundwater, Hydrogeochemistry
Descriptors:	None
Principal Investigators:	John Lenhart

Publication

Evaluating Colloid Release from Natural and Model Porous Media

2008 Annual Report

John J. Lenhart, Ph.D.
Dept. of Civil and Env. Eng. and Geod. Science
The Ohio State University
Columbus, OH 43210

Statement of Critical Regional or State Water Problem

The behavior of colloid-sized particles is of significant importance in natural and engineered systems. In natural systems, colloids comprised of singular and aggregated mineral, biological and organic components are ubiquitous in surface and subsurface waters. Due to their propensity to sorb otherwise sparingly soluble contaminants or in the case of biocolloids, inherent risk, their presence in water poses a potential health risk (McDowell-Boyer et al. 1986; McCarthy and Zachara 1989; Ryan and Elimelech 1996). Colloidal interactions are also important in water and wastewater treatment, chromatographic separation, oil production, extractive metallurgy, lubrication, coating and cleaning (Osipow 1962; Yao et al. 1971; Hiemenz 1986). Consequently, the physical and chemical processes that govern colloid interactions with surfaces have been extensively studied, and significant progress toward identifying processes responsible for colloid deposition has been made (e.g., Elimelech and O'Melia 1990; Song and Elimelech 1993; Lenhart and Saiers 2002; Lenhart and Saiers 2003; Tufenkji and Elimelech 2005). However, considerable uncertainty remains about the mechanisms that govern colloid interactions under unfavorable conditions, characterized by systems with like-charged surfaces, particularly with regard to mechanisms responsible for reversible deposition and colloid release in porous media (Kretzschmar et al. 1999). Knowledge of the fundamental processes that control the deposition, release and subsequent transport of colloidal particles and associated contaminants is crucial to maintaining the quality of ground water that the nearly five million residents of the Ohio (OhioEPA 2000) rely on for their daily needs.

Research Objective

The objective of this research is to evaluate the extent and kinetics of colloid release in water-saturated porous media under conditions selected to promote unfavorable DLVO interactions. The work will couple laboratory-scale experimental work with mathematical models to test existing theory and approaches to model colloid transport. Results of this research will be used to (1) evaluate the importance of the secondary minimum in reversible colloid deposition in systems with like-charged surfaces, (2) test the influence of system conditions (e.g., porous media, porewater velocity, porewater composition and colloid size) on reversible deposition, and (3) test the rigor of existing approaches that account for non-DLVO deposition (e.g., Tufenkji and Elimelech 2004) and examine their application to describe colloid release. Such information is needed to accurately predict colloid mobility and appropriately evaluate filtration technologies for their removal from source waters. Two overarching questions drive this research. They are:

- To what extent does reversible deposition depend upon the presence of the secondary minimum?
- How do system conditions (e.g., grain size, solute composition) influence reversible deposition?

Methods and Procedures

The deposition and mobilization of colloids will be evaluated in a series of bench-scale column experiments. Each experiment will consist of two stages, a deposition stage and a mobilization stage. During the deposition stage, a solution comprised of the colloids, suspended in a solution containing simple electrolytes (e.g., 0.01 M NaCl at pH 8), will be introduced into the column as a pulse. The concentration of the electrolyte and the valence of the cation in the influent suspension will be varied between experiments and a suite of experimental conditions will be tested in order to prepare columns that have different retained colloid profiles. Colloids deposited in the column during the first stage will be mobilized through a single, or through successive step-changes in the porewater electrolyte in the second stage. At the conclusion of each experiment, and for some experiments at the conclusion of the deposition stage the porous media will be extruded from the column and the profile of retained colloids will be measured.

Preparation and Characterization of Experimental Materials. Soda-glass beads and/or quartz sand will be used as the porous medium in all experiments. At least two fractions will be isolated for use with nylon sieves. As received, the media may be coated with metal oxides (Fe, Al and Ti) and trace quantities of organics. These impurities will be removed because they may influence surface charge characteristics and thus may promote colloid deposition (Litton and Olson 1993). Upon cleaning, the size and surface charge of the media will be evaluated via scanning electron microscopy and electrophoretic mobility measurements of native colloids (or streaming potential), respectively.

Surfactant-free fluorescent spherical latex particles will be used in all experiments as the colloidal phase. Carboxyl-modified surfaces are commonly used and the sizes chosen will depend upon whether deposition within the primary or secondary minima is to be accentuated. For example, Tufenkji and Elimelech (2005) evaluated the transport of 63, 320 and 3000 nm latex particles through 328 μm soda glass beads as a function of pH and ionic strength. Their results suggest that deposition within the primary minimum is highly unlikely for the 3000 nm particles, but possible for the same particles within secondary minimum. For the 63 nm particles, however, it is expected that conditions favor deposition within the primary minimum. Based on this interpretation, I suspect that compared to the 63 nm particles that the 3000 nm particles would be more amenable to release.

The manufacturer-reported diameter will be confirmed by dynamic light scattering. Latex colloid suspensions will be prepared by adding aliquots of a concentrated stock to the electrolyte solution to achieve the target colloid concentration. The average zeta-potential of the colloids in the different electrolyte solutions will also be determined on the basis of measured electrophoretic mobilities and the tables of Ottewill and Shaw (1972) or the Smoluchowski equation (Hunter 1981).

Column Design. Experiments on the transport of the latex microspheres follow the methods outlined by Lenhart and Saiers (2003). Glass chromatography columns with an internal diameter of 4.8 cm or 2.4 cm and PTFE end fittings will be used to contain the porous media. Depending

upon the desired flowrate a digital peristaltic pump or liquid chromatography pump will be used to control the flow of colloid and electrolyte solutions. The pump will be positioned at the base of the vertically oriented columns and the flow will be directed downward. Each experiment will use a fresh column prepared by wet-packing methods (Lenhart and Saiers 2003). The column will be packed to a predetermined height, and vibration will be used during packing to minimize air entrapment and the formation of layers. The porosity and pore-volume of each packed column will be measured using standard methods.

Column Experiment Methodology - Stage 1: Colloid Deposition. Each packed column will be pre-equilibrated with the electrolyte solution by pumping approximately 10 – 20 pore volumes of colloid-free electrolyte solution through the column prior to commencing the experiment. Colloid concentrations will be monitored in the column effluent during this period to verify that native colloid mobilization is negligible. The equilibration period will cease when the effluent pH matches that of the influent solution. Following column pre-equilibration, a suspension of latex colloids in electrolyte solution will be pumped into the column for a specific period of time (e.g., 2.5 pore volumes), whereupon the colloid-free electrolyte solution will be redirected into the column. Effluent colloid concentrations will be monitored in effluent samples collected with a fraction collector based upon fluorescence intensity or UV/Vis absorption, depending upon the particle size. Experiments will be conducted for different packing heights, electrolyte concentrations, porewater velocity and colloid concentration.

Column Experiment Methodology - Stage 2: Colloid Mobilization. Colloid mobilization will be induced at the conclusion of the deposition stage, when the effluent colloid concentrations return to baseline levels, by perturbing the composition of the electrolyte solutions to increase repulsive double-layer interactions between the colloid and media surfaces (e.g., by diluting electrolyte concentration). Successive perturbations will be examined, depending upon the initial conditions, as will the magnitude of the change in the electrolyte composition. The concentration of the electrolyte in the effluent will be monitored using a conductivity probe or specific ion electrode.

Measuring Retained-Colloid Profile. At the conclusion of each experiment the columns will be drained, disassembled, and the column packing will be extruded in order to measure the profile of retained colloids. A procedure developed by Bolster et al. (1999) will be followed. Upon extrusion, the porous media will be separated into sections approximately 1-cm in depth. These sections will be transferred into centrifuge tubes and appropriate volumes of 1 mM NaOH will be added. The samples will be equilibrated end-over-end for several hours to effect colloid release and then vigorously shaken using a vortex mixer to disperse the colloids throughout the solution. Aliquots of the supernatant will be removed, filtered (if necessary) and analyzed by fluorescent emission or UV/vis absorption. The solids will then be rinsed several times, oven-dried and weighed.

Interaction potential. The basic framework used in estimating the net or total potential energy between suspended colloidal particles or between colloidal particles and collector surfaces follows DLVO theory by summing van der Waals forces (ϕ_{VDW}) and electrostatic double layer forces (ϕ_{EDL}) (Derjaguin and Landau 1941; Verwey and Overbeek 1948). Hogg et al. (1966) derived expressions for electrostatic double layer interactions (ϕ_{EDL}) between two surfaces separated by a solution containing dissolved ions using a linearized approximation of the Poisson-Boltzmann equation. Although Hogg et al. (1966) stipulate the approximation is appropriate for surface potential less than 60 mV, Russel et al. (1989) state that it remains valid up to electrolyte concentrations of 1 M and surface potentials of 200 mV. Equations are

available for both sphere-plate and sphere-sphere interactions, and the expression for two non-identical spheres is given by (Hogg et al. 1966). Van der Waals forces, resulting from the interaction of dipoles, can be estimated assuming pair-wise additivity of the interatomic potentials (Hamaker 1937). At separation distances between the two surfaces greater than a few nanometers, the original Hamaker approach must be modified to account for a reduction in ϕ_{VDW} due to phase-shift between dipoles. To estimate the retarded ϕ_{VDW} I plan to use the expression of Gregory (1981). This equation was originally intended for separation distances less than $0.2r_C$ (Gregory 1981), but its accuracy can be verified for greater separation distances by comparison to the more rigorous expression for retarded ϕ_{VDW} from Czarnecki (1979). The total interaction energy is determined by summing the expressions for electrostatic and van der Waals interactions.

Model for Colloid Transport in Saturated Porous Media in Steady-State Conditions. The model presented by Lenhart and Saiers (2003) will be used to evaluate colloid transport. This model ties colloid release to a critical solute concentration where the barrier to colloid release vanishes. It couples equations to account for the transport of solute and colloids with a mass balance equation to account for the deposition and subsequent release of colloids. To account for distributed release of colloids as a function of solute concentration the model assumes surface irregularities in terms of potential or shape induce heterogeneities in the interaction energies between deposited colloids and the mineral grains. This heterogeneity is accounted for by dividing the immobile-phase colloid population into a series of compartments, where each compartment releases colloids at a characteristic critical solute concentration. The model can describe (1) the transport and deposition of colloids, (2) the consequent profile of the deposited colloids, (3) solute transport, (4) colloid release coupled to porewater solute concentrations, and (5) colloid release across a range in porewater solute compositions.

Principal Findings

The start of this project was delayed due to difficulties in locating and hiring a qualified graduate student to perform the work. Students were targeted and offers were extended in 2007, but these offers were declined and unfortunately an acceptable student was unable to be hired. Because of this, a no-cost extension was applied for in the latter stages of 2007. This request was granted and the duration of the project was extended to September 9, 2009. A new graduate student has been located and accepted an offer to work on this project starting October 1, 2008.

References

Bolster, C. H., A. L. Mills, G. M. Hornberger, and J. S. Herman (1999). *Water Resources Research*, 35(6): 1797-1807.

Czarnecki, J. (1979). *Journal of Colloid and Interface Science*, 72(2): 361-362.

Derjaguin, B. V. and L. D. Landau (1941). *Acta physicochim. URSS*, 14: 633-662.

Elimelech, M. and C. R. O'Melia (1990). *Environmental Science and Technology*, 24: 1528-1536.

Gregory, J. (1981). *Journal of Colloid and Interface Science*, 83(1): 138-145.

Hamaker, H. C. (1937). *Physica*, 4: 1058-1072.

Hiemenz, P. C. (1986). Principles of Colloid and Surface Chemistry. New York, Marcel Dekker, Inc.

Hogg, R., T. W. Healy, and D. W. Fuersteneau (1966). *Transactions of the Faraday Society*, 62: 1638-1651.

Hunter, R. J. (1981). Zeta Potential in Colloid Science, Principles and Applications. London, Academic Press.
Kretzschmar, R., M. Borkovec, D. Grolimund, and M. Elimelech (1999). *Advances in Agronomy*, 66: 121-193.
Lenhart, J. J. and J. E. Saiers (2002). *Environmental Science and Technology*, 36: 769-777.
Lenhart, J. J. and J. E. Saiers (2003). *Environmental Science and Technology*, 37: 2780-2787.
Litton, G. M. and T. M. Olson (1993). *Environmental Science and Technology*, 27: 185-193.
Litton, G. M. and T. M. Olson (1996). *Colloids and Surfaces A*, 107: 273-283.
McCarthy, J. F. and J. M. Zachara (1989). *Environmental Science and Technology*, 23: 496-502.
McDowell-Boyer, L. M., J. R. Hunt, and N. Sitar (1986). *Water Resources Research*, 22(13): 1901-1921.
OhioEPA (2000). Ohio's Ground Water Quality 2000 305(b) Report, Ohio Environmental Protection Agency Division of Drinking and Ground Waters.
Osipow, L. I. (1962). Surface Chemistry. New York, Reinhold Publishing Co.
Ottewill, R. H. and J. N. Shaw (1972). *Journal of Electroanalytical Chemistry and Interfacial Electrochemistry*, 37: 133-142.
Russel, W. B., D. A. Saville, and W.R. Schowalter (1989). Colloidal Dispersions. Cambridge, Cambridge University Press.
Ryan, J. N. and M. Elimelech (1996). *Colloids and Surfaces A*, 107: 1-56.
Song, L. and M. Elimelech (1993). *Colloids and Surfaces A*, 73: 49-63.
Tufenkji, N. and M. Elimelech (2004). *Langmuir*, 20: 10818-10828.
Tufenkji, N. and M. Elimelech (2005). *Langmuir*, 21: 841-852.
Tufenkji, N. and M. Elimelech (2005). *Environmental Science and Technology*, 39: 3620-3629.
Verwey, E. J. W. and J. T. G. Overbeek (1948). Theory of the Stability of Lyophobic Colloids. Amsterdam, Elsevier.
Yao, K.-M., M. T. Habibian, and C.R. O'Melia (1971). *Environmental Science and Technology*, 5(11): 1105-1112.

Information Transfer Program

The Ohio Water Resources Center (WRC), at Ohio State University, conducted a number of activities to transfer water related information to a wide range of state, federal, county, and municipal agencies, to the private sector, academic community, students, and to private citizens throughout Ohio. Specific activities included,

- preparation of information for the web site of the Ohio Water Resources Center and maintenance of the web site

- administration of a Special Water and Wastewater Treatment Grants Competition funded through the Ohio Water Development Authority

- administration of the 104(B) In-State Competition and the 104(G) National Competitive Grants Program

- encouraged investigators of projects funded through the Ohio WRC to develop publications in peer-reviewed journals and other outlets

- continued administrative support for the Water Management Association of Ohio (WMAO) and associated WMAO meetings, conferences, and division activities

- support for Ohio Water Education Program, especially Project WET (Water Education for Teachers)

- participation of both directors in the Future Engineers Summer Camp (FESC) which focuses on introducing 8th grade girls to careers in various areas of engineering, including water resources and environmental engineering

- responding to questions from the public regarding water resources issues in the state of Ohio

- organized Ohio American Water Works Association (AWWA) South East district section meeting at Ohio State University to facilitate transfer of research results to the water treatment profession.

Student Support

Student Support					
Category	**Section 104 Base Grant**	**Section 104 NCGP Award**	**NIWR-USGS Internship**	**Supplemental Awards**	**Total**
Undergraduate	5	0	0	0	5
Masters	2	0	0	0	2
Ph.D.	1	0	0	0	1
Post-Doc.	0	0	0	0	0
Total	8	0	0	0	8

Notable Awards and Achievements

Publications from Prior Projects

1. 2005OH16B ("Transport and Fate of Iron Nanoparticles in Groundwater") - Articles in Refereed Scientific Journals - Welch, R. and Riefler, R.G. in press. Estimating treatment capacity of nanoscale zero-valent iron reducing 2,4,6-trinitrotoluene. Environ. Eng. Sci.
2. 2005OH26B ("USE OF PERSULFATE AND PEROXYMONOSULFATE OXIDANTS FOR THE DESTRUCTION OF GROUNDWATER CONTAMINANTS") - Dissertations - Hyeok Choi, 2007, Novel Preparation of Nanostructured Titanium Dioxide Photocatalytic Particles, Films, Membranes, and Devices for Environmental Applications, PhD dissertation, University of Cinncinatti.
3. 2005OH26B ("USE OF PERSULFATE AND PEROXYMONOSULFATE OXIDANTS FOR THE DESTRUCTION OF GROUNDWATER CONTAMINANTS") - Dissertations - Aditya Rastogi, 2008, Sulfate Radical-Based Environmental Friendly Chemical Oxidation Processes for Destruction of 2-Chlorobiphenyl (PCB) and Chlorophenols (CPs), MS thesis, University of Cinncinatti.
4. 2005OH26B ("USE OF PERSULFATE AND PEROXYMONOSULFATE OXIDANTS FOR THE DESTRUCTION OF GROUNDWATER CONTAMINANTS") - Articles in Refereed Scientific Journals - Qiujing Yang, Hyeok Choi, Yongjun Chen and Dionysios D. Dionysiou, Heterogeneous Activation of Peroxymonosulfate by Supported Cobalt Catalysts for the Degradation of 2,4-Dichlorophenol in Water: The Effects of Support, Cobalt Precursor, and UV Radiation, Applied Catalysis B: Environmental 77 (3/4) (2008) 300-307.
5. 2005OH26B ("USE OF PERSULFATE AND PEROXYMONOSULFATE OXIDANTS FOR THE DESTRUCTION OF GROUNDWATER CONTAMINANTS") - Articles in Refereed Scientific Journals - Aditya Rastogi, Souhail R. Al-Abed, Dionysios D. Dionysiou, Effect of Inorganic, Synthetic and Naturally Occurring Chelating Agents on Fe(II) Mediated Advanced Oxidation of Chlorophenols, Submitted for Publication (now in revision).
6. 2005OH26B ("USE OF PERSULFATE AND PEROXYMONOSULFATE OXIDANTS FOR THE DESTRUCTION OF GROUNDWATER CONTAMINANTS") - Articles in Refereed Scientific Journals - Qiujing Yang, Hyeok Choi, Souhail R. Al-Abed, and Dionysios D. Dionysiou, Iron-Cobalt

Bimetallic Nanocatalysts: Heterogeneous Peroxymonosulfate Activation, Cobalt Leaching, and Ferromagnetic Properties for Environmental Applications, Submitted for Publication.

7. 2005OH26B ("USE OF PERSULFATE AND PEROXYMONOSULFATE OXIDANTS FOR THE DESTRUCTION OF GROUNDWATER CONTAMINANTS") - Conference Proceedings - Dionysios D. Dionysiou*, George P. Anipsitakis, Aditya Rastogi, Qiujing Yang, and Souhail Al-Abed, Sulfate Radical-Based Advanced Oxidation Processes. Invited Lecture at the Special ACS and AIChE Symposium on Applied Chemistry and Engineering, Division of Industrial and Engineering Chemistry Research, paper 35, 233rd American Chemical Society National Meeting (ACS), March 25-29, 2007, Chicago, Illinois.
8. 2005OH26B ("USE OF PERSULFATE AND PEROXYMONOSULFATE OXIDANTS FOR THE DESTRUCTION OF GROUNDWATER CONTAMINANTS") - Conference Proceedings - Aditya Rastogi*, Souhail R. Al-Abed, Dionysios D. Dionysiou, Destruction of PCBs Using Sulfate Radical-based Advanced Oxidation Processes. Oral Presentation at the Symposium on Sustainability in Water Supply: Advances in Oxidation Processes for Water Treatment, Division of Sustainability of Energy, Food and Water, paper 151, 233rd American Chemical Society National Meeting (ACS), March 25-29, 2007, Chicago, Illinois.
9. 2005OH26B ("USE OF PERSULFATE AND PEROXYMONOSULFATE OXIDANTS FOR THE DESTRUCTION OF GROUNDWATER CONTAMINANTS") - Conference Proceedings - Qiujing Yang and Dionysios D. Dionysiou*, Heterogeneous Activation of Oxone Using Nanoparticles Co/TiO2. Poster Presentation at The 12th International Conference on Advanced Oxidation Technologies for Treatment of Water, Air and Soil (AOTs-12), Sept. 25-28, 2006, Pittsburgh, Pennsylvania.
10. 2006OH34B ("Characterizing and Controlling Membrane Biofouling") - Articles in Refereed Scientific Journals - Kai Zhang, Hyeok Choi, Dionysios Dionysiou, and Daniel Oerther, Application of Membrane Bioreactors in the Preliminary Treatment of Early Planetary Base Wastewater for Long Duration Space Missions, Water Environment Research (Submitted for Special Focus Issue on Bacterial Aggregation and Flocculation) (Now in revision).
11. 2006OH34B ("Characterizing and Controlling Membrane Biofouling") - Conference Proceedings - Kai Zhang, Hyeok Choi, Dionysios D. Dionysiou, and Daniel B. Oerther, Application of Membrane Bioreactors in the Preliminary Treatment of Early Planetary Base Wastewater for Long Duration Space Missions. Proceedings of WEFTEC 2006, the 79th Annual Water Environment Federation (WEF) Conference and Exposition, pp. 62-81, October 21-26, 2006, Dallas, Texas.
12. 2006OH34B ("Characterizing and Controlling Membrane Biofouling") - Conference Proceedings - Kai Zhang, Hyeok Choi, Dionysios D. Dionysiou, Daniel B. Oerther, Influence of Loading Modes on Sludge Properties in Membrane Bioreactors Treating a Synthetic Early Planetary Base Wastewater. Proceedings of the 37th Mid-Atlantic Industrial and Hazardous Waste Conference, March 21-23, 2007, Cincinnati, OH.